Nanostructured and Heterostructured 2D Materials for Thermoelectrics

Qin-Yi Li[1,5,*], Qing Hao[2,*], Tianhui Zhu[3], Mona Zebarjadi[3,4,*], Koji Takahashi[1,5]

[1]Department of Aeronautics and Astronautics, Kyushu University, Fukuoka 819-0395, Japan

[2]Department of Aerospace & Mechanical Engineering, University of Arizona, 1130 N Mountain Ave, Tucson, AZ, 85721, USA

[3]Department of Electrical and Computer Engineering, University of Virginia, Charlottesville, Virginia, 22904, USA.

[4]Department of Materials Science and Engineering, University of Virginia, Charlottesville, Virginia, 22904, USA.

[5]International Institute for Carbon-Neutral Energy Research (WPI-I2CNER), Kyushu University, Japan

[*]Corresponding authors, Qin-Yi Li: qinyi.li@aero.kyushu-u.ac.jp

Qing Hao: qinghao@arizona.edu

Mona Zebarjadi: m.zebarjadi@virginia.edu

Abstract

The rapid development in the synthesis and device fabrication of 2D materials provides new opportunities for their wide applications in fields including thermoelectric energy conversion. As one important research direction, the possibly poor thermoelectric performance of the pristine 2D materials can be dramatically improved with patterned nanoporous structures and/or heterostructures. This article reviews the recent advancement along this direction, with emphasis on both fundamental understanding and practical problems.

Keywords: 2D materials, thermoelectrics, nanostructure, heterostructure

1. Introduction

Solid-state thermoelectric devices, which directly convert heat into electricity or oppositely, can be utilized to address two significant issues in the development of emerging micro- and nano-scale devices. One issue is how to power the ubiquitous sensors in the future IoT (Internet of Things) society, where the thermoelectric power generator utilizing the Seebeck effect is one of the most promising self-powering technologies to harvest energy from waste heat and the environment. The second is how to dissipate the increasingly high heat flux from a hot spot in the large-scale integration, where a solid-state Peltier cooler can play an irreplaceable role in efficient heat removal. In the context of power generation, the performance of thermoelectric material is evaluated by a well-defined dimensionless property, figure of

merit, *i.e.* $ZT = S^2\sigma T/(k_e+k_l) = PFT/k$, where $S = -\Delta V/\Delta T$ is the Seebeck coefficient (thermopower), σ the electrical conductivity, T the absolute temperature; k is the thermal conductivity that can be divided into the electronic part, k_e, and the lattice part, k_l; and $PF = S^2\sigma$ is defined as the power factor (*PF*) that evaluates the ability to output a high electric power with an applied temperature difference or oppositely [1]. A good thermoelectric material for power generation requires a high *PF*, and at the same time a low k to minimize the conduction heat leakage and thus maintain the temperature difference. A high ZT is also desired for a Peltier refrigerator to pump heat from a cold source to a hot end. However, both a high *PF* and a high k are beneficial in the context of thermal management where heat is transferred from a hot spot to a heat sink [2]–[4]. Note that the product of *PF* and T, i.e. *PFT*, has the same unit with the thermal conductivity of Watt per meter per Kelvin. Thus, *PFT* represents the ability of active cooling using the Peltier effect, while k represents the ability of passive cooling [2],[5]. For either power generation or thermal management, we need to manipulate S, σ, and k for improved performance, which has been particularly challenging for decades because these transport properties are generally intertwined.

There are mainly two strategies to enhance the thermoelectric figure of merit: (1) to suppress phonon transport without significantly affecting electron transport, and (2) to engineer the band structure for a higher *PF*. It is beneficial to increase the number of modes within the Fermi window near the band edges, which can be realized by reducing the dimensionality [6],[9]. A sharp density of states (DOS) profile at the band edge is expected in 2D materials, and superior electron mobility has been observed in many 2D crystals like graphene and 2D transition metal dichalcogenides (TMDCs), which is one reason why 2D materials are promising for thermoelectric applications. Another advantage of 2D materials is the environment-friendliness and flexibility. Traditional thermoelectric materials with $ZT > 1$ usually involve toxic or rare elements like Bi, Te, Pb, and Ag, which has long hindered their large-scale deployment due to the high cost and environmental harm. Besides, these hard materials are not suitable for energy harvesting in small-scale, flexible devices. Therefore, 2D layered materials with non-toxic, low-weight, and flexible features have attracted increasing attention for thermoelectric applications that are integrated into small-scale and flexible devices.

Many 2D materials in the pristine form indeed possess a relatively high *PF*. For pristine graphene without doping, the Fermi level is at the Dirac point or charge neutrality point so that S and $S^2\sigma$ are both zero. [27] The sign of the Seebeck coefficient is changed across the charge neutrality point, where the majority charge carrier switches from electrons to holes. With an applied gate voltage to optimize the Fermi level, semimetal graphene exhibits an improved Seebeck coefficient of about 80 μV/K [1],[10],[11], but its *PF* can be up to 10 $mW/m\cdot K^2$ due to the extremely high mobility [10]. Semiconducting bilayer MoS_2 can exhibit a *PF* up to 8.5 $mW/m\cdot K^2$ [12], about twice that of bulk Bi_2Te_3. However, the figure of merit of the existing pristine 2D materials is orders of magnitude lower than commercial thermoelectric materials such as Bi_2Te_3 alloys. For example, the *ZT* value of pristine graphene [10] and 2D MoS_2 are only on the order of 10^{-3} and 10^{-2}, respectively. Therefore, it is desired to independently engineer both electron and phonon transport for improved thermoelectric performance of 2D materials.

Two approaches can be used to modify the structure of a 2D system and alter the thermoelectric properties accordingly. First, a 2D sheet can be patterned into a nanostructure like a nanoribbon or a porous mesh through lithographical or special synthetic approaches. As pioneered by Hicks and Dresselhause in 1993 [13],[14], nanostructures can alter the band structure. In later studies, suppressed phonon transport is often found as another important benefit for nanostructured materials with strong boundary or interface phonon scattering. [15],[16] For charge carriers with usually shorter mean free paths (MFPs) than those for phonons, they are less scattered so that bulk-like electrical properties can be preserved. In general, S, σ, and k can be hopefully decoupled and independently manipulated by careful structure design. Second, different 2D crystals can be stacked layer by layer to establish a van der Waals heterostructure where the band structure as well as phonon transport can be tuned by the van der Waals interfaces, promisingly leading to enhanced thermoelectric performance. Besides, the thermoelectric properties of 2D crystals can be significantly modified by the type of the substrate, and the number of layers. Up to now, researchers have exfoliated or synthesized a few dozen of 2D crystals, with at least one thousand more still waiting to be discovered [17]–[19], while the nanostructuring and stacking approaches can yield infinite possibilities for constructing a 2D system. The only limitation for tuning the thermoelectric properties is our imagination and a rational approach of the structure design.

In recent years, the thermoelectric studies of 2D materials have been reviewed by several articles [1],[2],[20]–[27] from different angles including an emphasis on how to tune the Fermi level. The present review is devoted to the tunability of both electron and phonon transport that is benefited from the structure manufacturability of 2D materials, including critical reviews of the most updated experimental and theoretical progress. We will start from a summary of the thermoelectric properties of pristine 2D materials, and then successively discuss the nanostructured and heterostructured 2D materials for the manipulation of thermoelectric properties and give our perspectives in the last section.

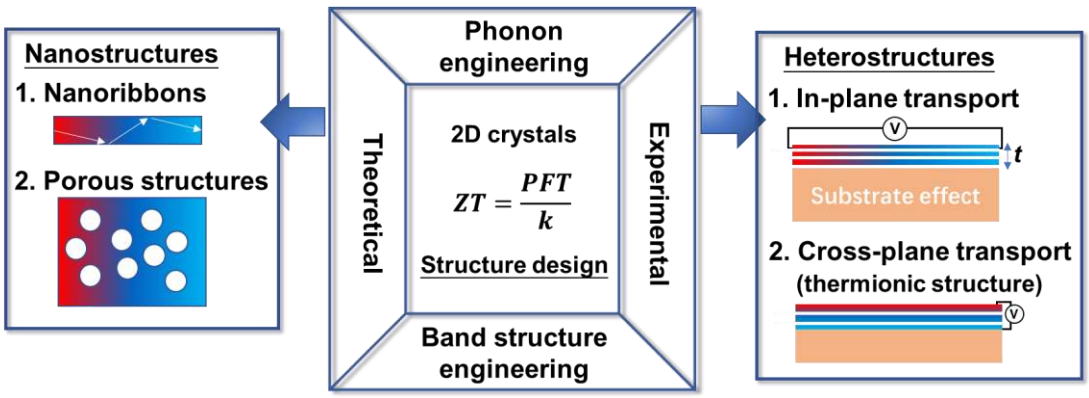

Fig. 1 Concept and outline of this review.

2. Thermoelectric properties of pristine 2D materials

In this section, the thermoelectric properties of 2D materials are reviewed. It should be noted that the possibly low *ZT* values of these pristine materials may be largely improved with the nanostructuring approach that will be discussed in later sections.

2.1 Thermoelectric properties of single- and few-layer graphene

Monolayer graphene is an intrinsic semimetal with a gapless band structure. Several measurements of monolayer graphene supported on SiO_2 have confirmed a Seebeck coefficient of about 80 μV/K under an optimized gate voltage to tune the Fermi level [1], [10], [11],[29],[30] and an electrical conductivity on the order of 10^6 S/m at room temperature (RT) for high-quality samples [10]. A high *PF* up to about 10 mW/m·K^2 was reported for exfoliated single-layer graphene on a suspended SiO_2 thin film, [10] which is more than twice that of commercial bulk Bi_2Te_3 alloys. However, pristine graphene has an extremely high thermal conductivity of around 3000 W/m·K in the suspended form [10]–[35] and 600 W/m·K in the SiO_2-supported form [10] at RT leading to a very small *ZT* value on the order of 10^{-3}. Here, the considerably reduced thermal conductivity of the supported graphene is caused by the suppression of flexual phonons from the amorphous substrate. Due to the small *ZT* value, large-area pristine monolayer graphene is not suitable for thermoelectric power generation, but the relatively high *PF* and remarkably high thermal conductivity can be utilized for efficient active cooling of a hot spot [2].

Bulk graphite is also a semimetal with a high thermal conductivity up to 2000 W/m·K. For free-standing graphene, the thermal conductivity increases from the graphite value to the monolayer value as the thickness decreases. However, the thermal conductivity of supported graphene, which is suppressed by the substrate coupling, increases with increasing layer numbers and can recover to the graphite value when the thickness is more than 30 layers [31]. As for the bandgap, bilayer and trilayer graphene can exhibit a nonzero bandgap and band strcucture that can be widely tuned by the electric field or twist angle, which involves profound physics [36]–[39] and can be beneficial for enhancing the Seebeck coefficient. The maximum Seebeck coefficient of bilayer graphene without bandgap tuning was measured to be about 100 μV/K at 250 K [40], while the maximum Seebeck coefficient of bilayer graphene gapped by the electric field was reported to be up to 180 μV/K at 100 K [41],[42]. Moreover, a recent theoretical work [43] reported a *ZT* value larger than unity in gapped bilayer graphene at an ultralow temperature of 1 K.

2.2 Thermoelectric properties of 2D TMDCs

TMDCs are a family of layered materials with a molecular formula of MX_2, where a transitional metal atom, M, is sandwiched by two chalcogen element atoms, X. The 2D forms of semiconducting TMDCs represented by 2H-type MX_2 (M = Mo, W; X = S, Se) have attracted intense research efforts for their potential applications in nanoelectronics and optoelectronics [44], and many studies have exploited their potentially high thermoelectric performance due to their direct bandgaps and much lower thermal conductivities than that for graphene [45]–[71].

The thermal conductivities of bulk MoS_2 crystals have been measured to be 85–110 W/m·K in the in-plane direction and 2.0±0.3 W/m·K in the through-plane direction at RT using the pump-probe metrology based on the magneto-optic Kerr effect [53]. A variable-spot-size time-domain thermoreflectance (TDTR) approach [54] was employed to systematically measure the in-plane and the through-plane thermal conductivities of bulk MX_2 (M = Mo, W; X = S, Se) at 80-300 K. At RT, the in-plane thermal conductivity of the measured TMDCs exhibits the following decreasing order of WS_2 (120 W/m·K) > MoS_2 (82 W/m·K) > WSe_2 (42 W/m·K) > $MoSe_2$ (35 W/m·K), the trend of which agrees well with first-principles calculations [56]. Another TDTR measurement of disordered, layered WSe_2 crystals yielded ultralow out-of-plane thermal conductivity of 0.05 W/m·K at RT [55]. These accurate measurements of the bulk crystals provide a baseline for understanding thermal transport in 2D TMDCs. The thermal conductivities of single- and few-layer TMDCs have been reported by a few Raman-based [57]–[63] and micro-bridge-based [64]–[66] measurements, but the limited data scattered in a large range (between ～15 and ～100 W/m·K at RT for monolayer MoS_2). Meanwhile, careful MD simulations [68],[50], first-principles [67] and BTE [69] calculations agreed well on the in-plane thermal conductivities of 2D MoS_2, which are above 100 W/m·K for the monolayer, decrease with increasing thickness and saturate at the trilayer to be about 80 W/m·K. The first-principles calculations [67] reported the RT thermal conductivities of 2H-type TMDC monolayers as 142 W/m·K for WS_2, 103 W/m·K for MoS_2, 54 W/m·K for $MoSe_2$, and 53 W/m·K for WSe_2. Moreover, this first-principles work found that the 1T-type TMDC monolayers represented by ZrS_2 possess a much lower thermal conductivity than the 2H-type monolayers [67]. Besides, Wan and co-workers [71] measured assembled TiS_2 layers with organic intercalation, which exhibited an ultralow in-plane thermal conductivity of 0.12 W/m·K that is two orders of magnitude lower than both bulk and monolayer TiS_2, along with a high *PF* of 0.45 mW/ m·K^2, resulting in a *ZT* value up to 0.28 at 373 K.

As for the *PF*, Wu and co-workers [48] measured a very large Seebeck coefficient of up to 30 mV/K at RT in CVD monolayer MoS_2, which indicated its promising application in themoelectics. Hippalgaonkar and co-workers [12] measured exfoliated single- to tri-layer MoS_2, and obtained a Seebeck coefficient aroung -400 μV/K at a zero gate voltage, while the *PF* of bilayer MoS_2 was as high as 8.5 mW/m·K^2 at a carrier concentration of 1.06×10^{13}/cm^2. Another thickness-dependent study on exfoliated MoS_2/SiO_2 samples also confirms that the best *PF* occurs for bilayer MoS_2. [49] In addition, Li and co-workers [51] measured tunable bandgap in monolayer MoS_2 that changes with uniaxial strain at a modulation rate of up to ~136 meV/%, thus we may expect a even larger Seebeck coefficient in deformed MoS_2 as flexible thermoelectric applications. Besides MoS_2, Exfoliated 3L WSe_2 on SiO_2 shows a peak Seebeck coefficient of around 200 μV/K for electron conduction and around 250 μV/K for hole conduction at 300 K. [52] Its maximum PF reaches 3.7 mW/m·K^2 for p-type WSe_2 and about 3.2 mW/m·K^2 for n-type, corresponding to electrical conductivities of approximately 3×10^4 S/m and 1×10^4 S/m respectively. [52] We can combine the separately measured *PF* and thermal conductivity and estimate *ZT* to be about 0.02 for pristine MoS_2 and WSe_2.

2.3 Thermoelectric properties of 2D black phosphorene and layered tin selenide

2D black phosphorus (or phosphorene) is a narrow-bandgap semiconductor with a orthorhombic puckered honeycomb structure of phosphorus atoms, and has attracted great attention due to its high mobility and anisotropic properties [72]. The thermoelectric properties of phosphorene has attracted much attention and relatively high *ZT* values up to 2 have been theoretically reported [77]–[83]. Tin selenide (SnSe) layers possess the same puckered lattice structure and anisotropicity with black phosphorus, and the layered bulk SnSe with the 2D nature has been identified as one of the most high-performance thermoelectric materials with an unprecedented *ZT* value up to 2.6 at 923 K [84]-[88]. Thus, we can group phosphorene and SnSe as a family of materials with the same lattice structure that can be very promising candidates as environmentally-friendly 2D thermoelectric materials.

The thermal conductivity of black phosphorus (BP) nanosheets has been measured by the Raman optothermal method [73], time-domain thermoreflectance (TDTR) method [74], the two-probe micro-bridge method [75] and the four-probe method [76]. Unlike suspended graphene whose thermal conductivity increases with decreasing thickness, BP nanosheets exhibited a decreasing trend of thermal conductivity in all the three directions as the thickness decreases [76], which indicates that monolayer or few-layer BP can have higher *ZT* values than thick flakes due to both enhanced electrical conductivity and reduced thermal conductivity. For 138-552 nm-thick BP flakes at RT, the through-plane thermal conductivity was measured to be 4.0 W/m·K, and the highest in-plane thermal conductivities were 86 and 34 W/mK in the zigzag and armchair directions, respectively [74]. The Seebeck coefficient of 10–30 nm thick BP was measured to be up to ~400 μV/K near 300 K [82], and the *PF* of 40 nm thick BP was measured to be ~4.5 μW/cm·K^2 at 210 K [80]. Combining the experimental results of thermal conductivity and *PF*, the *ZT* value of BP flakes with tens of nanometers thickness can be estimated to be on the order of 10^{-3}, which indicates much room for the enhancement of thermoelectric performance. As for bulk single-crystal layered SnSe, Zhao and co-workers [84] measured ultralow thermal conductivities of less than 0.4 W/m·K at 923 K, Seebeck coefficients of up to ~550 μV/K at 300 K, and very high *ZT* values of larger than 2.3 at 723–973 K even without doping. We can expect an even lower thermal conductivity in single- or few-layer SnSe because it shares the same lattice structure with BP, and thus 2D SnSe can be a very promising thermoelectric material.

2.4 Thermoelectric properties of other 2D sheets

Researchers have identified some other 2D sheets as potential good thermoelectric materials, including 2D tellurium (tellurene) [90]–[92], and 2D KAgSe nanosheet [93] *etc.*, the bulk counterparts of which are usually outstanding thermoelectric materials.

Bulk trigonal Te is a p-type narrow-bandgap semiconductor with the *ZT* value up to unity around 600 K and ~0.15 at 300 K [89], and some theoretical studies [90],[91] indicated even higher thermoelectric performance for the 2D counterpart of Te due to the quantum confinement. Qiu and co-workers [92] measured the thermoelectric properties of 2D Te nanofilms with ~30-nm thickness and ~10 μm lateral sizes. With MEMS-based resistive thermometers, the RT Seebeck coefficient and *PF* of the Te nanofilm sample supported on SiO_2

were measured to be 413 μV/K and 31.7 μW/cm·K^2, respectively. The thermal conductivity of a suspended 2D Te sample was measured by the Raman optothermal method to be 1.5 W/m·K, half that of bulk Te. Eventually, the *ZT* value of ~30-nm thick Te nanofilms was up to 0.63 at 300 K, four times that of bulk Te.

Besides, the thermoelectric properties of atomically thin 2D KAgSe nanosheet was studied by first-principles calculations and the Boltzmann transport equation (BTE) [93], which predicted an ultralow thermal conductivity of 0.03 W/m·K at 700 K for the trilayer KAgSe and a very high *ZT* value up to 2.08. SnS_2 nanosheets with a thickness of several tens of nanometers were measured by a MEMS-based device for the thermoelectric properties [95]. As the thickness of the SnS_2 decreased, the electrical conductivity increasd while the thermal conductivity decreased, which leads to a *ZT* value up to 0.13 at 300 K, ~1,000 times that of bulk SnS_2. Shimizu and co-workers [96] measured an enhanced Seebeck coefficient in ZnO thin films with a thickness of several nanometers as compared to bulk ZnO. Hung and co-workers [97] conducted BTE and first-principles calculations for monolayer InSe and found a *PF* up to 50 mW/mK^2. In addition, using the density functional theory (DFT) and semiclassical BTE calculations, Sharma *et al.* [98] predicted enhanced *ZT* in As and Sb monolayers as compared to the bulk counterparts, and Yu *et al.* [99] predicted a peak *ZT* value of 1.84 at 800 K in single-layer p-type BiOBr. Wang and co-workers [110] studied another 2D carbon allotrope named graphyne using the first-principles calculations and the nonequilibrium Green's function (NEGF) formalism, and obtained a *ZT* value of 0.16 at RT that is much larger than that of graphene.

3. Nanostructured 2D materials for thermoelectrics

As observed in Section 2, some 2D materials like graphene may not be attractive for conventional thermoelectric applications. However, unfavorable properties like an ultrahigh thermal conductivity can be tailored by introducing 2D nanofeatures across the atomic-thick material, e.g., nanoribbons or periodic pores. This Section will summarize the major advancement in this important research direction.

3.1 Theoretical progress

To compute the lattice thermal conductivity, two major approaches are employed for 2D materials, namely first-principles calcualtions and molecular dynamics (MD) simulations. The accuracy of MD simulations can be largely improved with first-principles computed interatomic force constants [100]. Atomistic Green's function method [101],[156] can also be used in certain cases based on the computed phonon transmissivity across a structure. However, inelastic phonon scattering cannot be easily incorporated in this method.

For electrical properties, the required electronic band structures can be computed with first-principles calculations (unit cell of ~100 atoms or less) or tight binding modeling (unit cell of ~10 nm sizes or less). For electron conduction, both ballistic and diffuse regimes can be physically formulated by the Landauer approach [6],[7], by which the spectral electrical

conductivity per unit energy, $\sigma'(E)$, is formulated in terms of the energy (E)-dependent transmission of electrons, $\mathcal{T}_e(E)$, given by [6]

$$\sigma'(E) = \frac{L}{A}\frac{2e^2}{h}\mathcal{T}_e(E)M_e(E)(-\frac{\partial f_{FD}}{\partial E}) \quad (1)$$

where $M_e(E)$ is the energy-dependent number of modes that is proportionally related to the DOS of electrons, e the electron charge, f_{FD} the Fermi-Dirac distribution function, h the Planck constant, L the sample length and A the cross-sectional area. The electron transmission function, $\mathcal{T}_e(E)$, can be related to the energy-dependent MFP, $\lambda(E)$, by $\mathcal{T}_e(E) = \lambda(E)/(\lambda(E) + L)$. [102] The total electrical conductivity is then given by

$$\sigma = \int \sigma'(E)dE \quad (2)$$

The Seebeck coefficient, S, is derived to be [6]

$$S = -\frac{1}{eT}\frac{\int(E-E_F)\sigma'(E)dE}{\sigma} = -\frac{1}{eT}[\frac{\int E\mathcal{T}_e(E)M_e(E)(-\frac{\partial f_{FD}}{\partial E})dE}{\int \mathcal{T}_e(E)M_e(E)(-\frac{\partial f_{FD}}{\partial E})dE} - E_F] \quad (3)$$

where E_F is the Fermi energy. Accordingly, the Seebeck coefficient is determined by the difference between the average carrier energy and the Fermi level. The Seebeck coefficient decreases while the electrical conductivity increases with increasing Fermi level, and there exists a maximum PF at the optimized Fermi level somewhere near the band edge. Further, the electronic thermal conductivity, k_e, is formulated by

$$k_e = \frac{1}{e^2T}\int(E - E_F)^2\sigma'(E)dE - T\sigma S^2 \quad (4)$$

and the lattice thermal conductivity, k_e, which dominates thermal transport in semiconductors, can be parallelly formulated by the Landauer approach in terms of the transmission function of phonons [8]. Both electron and phonon transports can be scattered by defects, impurities, and boundaries, the effects of which are reflected in the MFPs or the transmission functions of phonons and electrons in the Landauer formalism.

For materials like graphene and boron nitride, particular attention should also be paid to the hydrodynamics of the phonon transport [103]–[106]. This occurs when the momentum-conserving normal process overshadows the resistive Umklapp process. In contrast with bulk materials, with hydrodynamic phonon transport only at extremely low temperatures [107], phonon hydrodynamics can be found in some 2D materials well above cryogenic temperatures. Similar phonon hydrodynamics is also claimed for graphite even above 100 K [108]. In this case, heat can propagate in the form of a damped wave and second sound can be hosted within the material. This interesting phenomenon should also be considered in the thermal design of nanostructured 2D materials, such as graphene nanoribbons [109].

3.1.1 Nanoribbons

Nanoribbons are strips of 2D materials with a width of approximately less than 100 nm. Different kinds of nanoribbon structures have been studied for thermoelectric properties, including graphene nanoribbons (GNRs) of various shapes [118]–[132], sp3-bonded graphane

nanoribbons [133], silicene and germanene nanoribbons [134]-[136], TMDC nanoribbons [137]–[139], phosphorene nanoribbons [140], and hybrid superlattice nanoribbons [141]–[147],[134]. Table 1 lists the reported *ZT* values of nanoribbons in the existing theoretical studies, which range from 0.1 to ~6 at RT.

All these studies reported both enhanced Seebeck coefficient due to the bandgap opening and drastically reduced thermal conductivity as compared with the bulk counterpart, which can be generally explained by phonon scattering with boundaries as well as the ballistic phonon transport because of the nanoscale sizes that are smaller than the phonon MFP [111]–[117]. For example, the phonon MFP of bulk graphene is up to ~300 nm [113] and thus the phonon scattering with the rough edges dominates the thermal resistance in a GNR with a width of less than 100 nm, while the ballistic phonon transport can be important in a GNR with a length of less than 300 nm and reduce the effective thermal conductivity. Generally, the thermal conductivity of nanoribbons with the same edge roughness decreases with decreasing ribbon width [112]. The edge roughness is the other important factor that determines the strength of phonon-edge scattering. Because the zigzag edge is more smooth than the armchair edge, which suggests a weaker phonon scattering with the zigzag edge, it was found that the perfect zigzag GNR has a larger thermal conductivity than the armchair ones with the same width [115],[117]. In practice, both experimental and theoretical studies also have demonstrated that the zigzag edges also have long-termed stability [114]. For instance, the edge of a hole with more armchair configuration initially would finally be stabilized with more zigzag configuration under electron beam irradiation. Interestingly, phonon scattering gets much stronger at atomically disordered zigzag edges of GNRs (Fig. 2 (a)), which can reduce the thermal conductivity by 10 fold as compared with that of perfect zigzag GNRs [119]. In addition to the phonon-edge scattering, phonon scattering with isotopes [123],[124] and bulk defects [118],[120],[133] has also been explored to further reduce thermal conductivity of nanoribbons. In the GNRs with non-uniform widths or assembled GNRs (Fig. 2 (b)–(d)), the GNR segments can have different phonon spectra and the phonon transport can be further suppressed due to the thermal boundary resistance between segments as well as the phonon localization [124]–[127]. Besides, it was found that the tensile strain can reduce the thermal conductivity of GNRs and thus increase the *ZT* value [128],[129]. In the superlattice nanoribbons consisting of hybrid 2D crystals (Fig. 3 (b), (c) and (f), [141]–[147]), the mechanisms of thermal conductivity reduction include the phonon-interface scattering and interference effects.

The electron transport, however, can be suppressed by the same boundary scattering as the phonon transport. For the enhancement of *ZT*, the point is how to design a sophisticated nanostructure that can suppress phonon transport much more strongly than electron transport by utilizing the disparate features of phonons and electrons. Especially, defects are inevitable in real samples and it is important to figure out the effects of defects on both electron and phonon transport. Several theoretical studies [118]–[120] have suggested that disorders at the edges can scatter phonons much more strongly than electrons in GNRs, which can lead to a higher ratio of electrical to thermal conductivities and thus a higher *ZT*. However, bulk defects inside the GNR suppress electron transport more significantly than phonons [118],[120], which can result in a decreased *ZT*. These results suggest that a clean GNR with rough edges but few bulk defects is preferred for thermoelectric applications. A more recent theoretical study [123]

demonstrated that isotopes and vacancies at the lowest electron density positions of GNRs can drastically reduce the thermal conductance without degrading the electrical conductance particularly in the low-energy region, which provides further guidance for sophisticated defect engineering in GNR thermoelectrics.

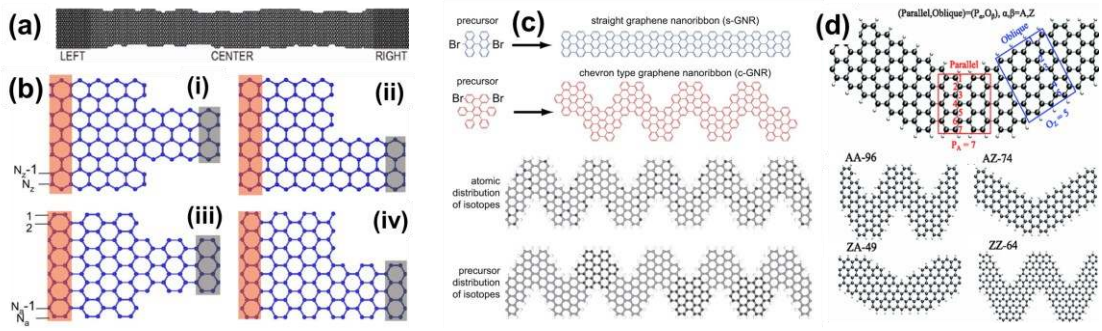

Fig. 2 Graphene nanoribbon (GNR) structures for enhanced thermoelectric performance. (a) An edge disordered zigzag GNR (adapted from [119]). (b) T-shaped and L-shaped, zigzag, and armchair GNRs (adapted from [126]). (c) Precursor or isotope-based bottom-up construction of straight and chevron type GNRs (adapted from [125]). (d) GNRs assembled to various structures (adapted from [130]).

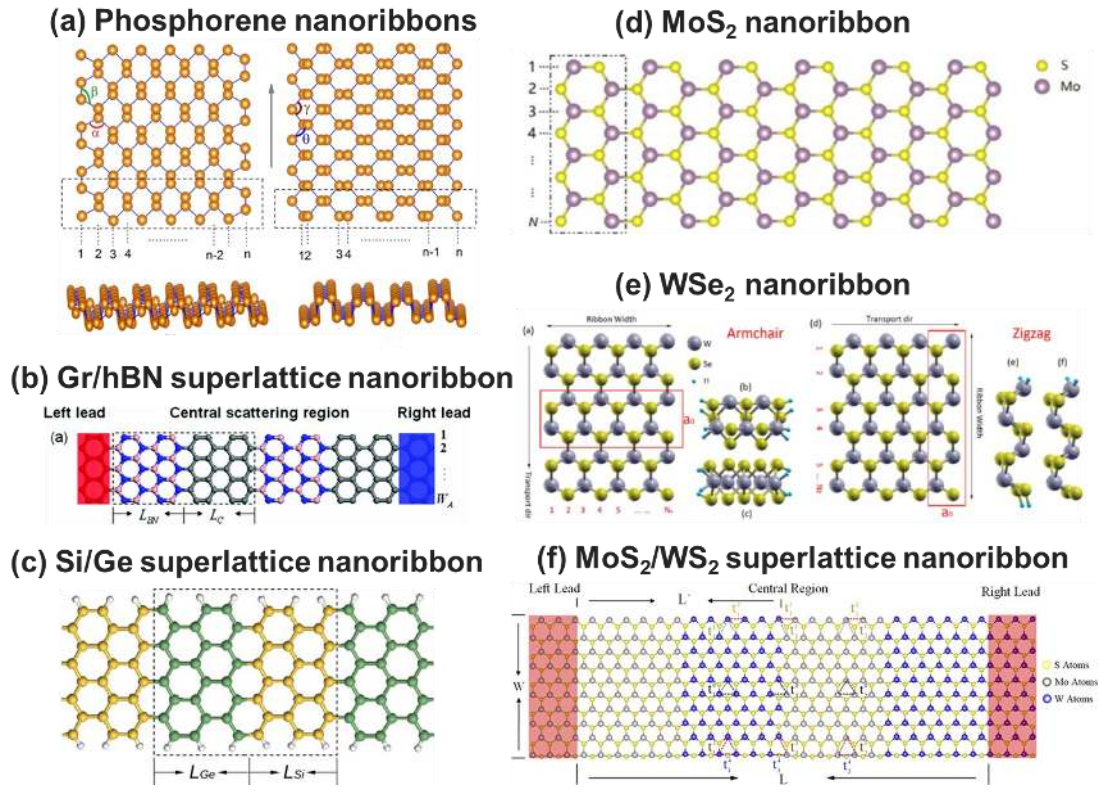

Fig. 3 Various nanoribbons explored for thermoelectric applications. (a) Phosphorene nanoribbons (adapted from [140]). (b) Graphene/boron nitride superlattice nanoribbons

(adapted from [145]). (c) Si/Ge superlattice nanoribbons (adapted from [134]). (d) MoS_2 nanoribbons (adapted from [137]). (e) WSe_2 nanoribbons (adapted from [138]). (f) MoS_2/WS_2 superlattice nanoribbon (adapted from [146]).

Table 1. *ZT* values reported in theoretical studies of nanoribbons

Material	Reference	Calculation method	Structure features	Max. *ZT*
GNR	Ouyang *et al.* (2009) [118]	NEGF	Width = 1.8 nm; varied edge disorder and vacancy	0.1 @ 300 K
GNR	Sevinçli *et al.* (2010) [119]	NEGF	Edge disordered zigzag GNRs (Fig. 2 (a))	4 @ 300 K
GNR	Karamitaheri *et al.* (2012) [121]	NEGF	Zigzag GNRs with line defects, substrate impurities & edge roughness	5 @ 300 K
GNR	Zheng *et al.* (2012) [122]	NEGF & MD	0.4-1.4 nm wide armchair and zigzag GNRs	6.0 @ 300 K
GNR	Tran *et al.* (2017) [123]	Green's function & Landauer theory	Width ~ 1 nm, isotopes & vacancies at the lowest electron density positions	2.5 @ 300 K
GNR	Tan *et al.* (2015) [124]	First-principles	Zigzag GNRs with gold atom chains at the edges	~1 @ 300 K, ~2 @ 500 K
GNR	Sevinçli *et al.* (2013) [125]	First-principles	Precursor/isotope-based straight/chevron type GNRs (Fig. 2 (c))	~2 @ 300 K 3.25@800 K
GNR	Pan *et al.* (2012) [126]	NEGF & Landauer theory	T- and L-shaped, varied chirality (Fig. 2 (b))	~0.6@300 K ~0.9@100 K
GNR	Yeo *et al.* (2013) [128]	DFT & Landauer theory	Strained armchair GNRs	~0.7@800 K
GNR	Mazzamuto *et al.* (2011) [127]	NEGF	Mixed chirality	~1 @300 K
GNR	Liang *et al.* (2012) [130]	DFT & semiempirical	GNR assembly (Fig. 2 (d))	~0.7@300 K
GNR	Mazzamuto *et al.* (2012) [131]	Green's function	Disordered edges & vacancies	0.4@300 K
GNR	Yan *et al.* (2012) [132]	NEGF	Hexagonal shapes with zigzag or armchair edges	~2@300 K
Graphane	Liang *et al.* (2009) [133]	DFT & NEGF	~1-to-5-nm wide	~2@300 K 5.8 @700 K
Silicene	Zberecki *et al.* (2013) [135]	First-principles	Zigzag edges, varied width	~2.5 @ 90 K
MoS_2	Fan *et al.* (2014) [137]	First-principles & BTE	Varied chirality and width (Fig. 3 (d))	2.7@ 300 K
WSe_2	Chen *et al.* (2016) [138]	First-principles	Varied chirality and width (Fig. 3 (e))	2.2 @ 300 K
WSe_2	Wang *et al.* (2017) [139]	First-principles & NEGF & BTE	Varied chirality and sizes	1.4 @ 300 K 2.1 @ 500 K
Phosphorene	Zhang *et al.* (2014) [140]	DFT	Zigzag and armchair NRs (Fig. 3 (a))	6.4 @ 300 K

Si, Ge, and hybrid	Yang *et al.* (2014) [134]	First-principles	Varied width and supercell length (Fig. 3 (c))	2.5 @ 300 K
Gr/hBN hybrid	Tran *et al.* (2015) [143]	Green's function	hBN attached to the sides of GNRs	0.8 @ 300 K 1.0 @ 100 K
Gr/hBN hybrid	Yang *et al.* (2012) [145]	NEGF	Varied width and periodic length (Fig. 3 (b))	~0.7@ 300 K
MoS_2/WS_2 hybrid	Zhang *et al.* (2016) [146]	NEGF & MD & First-principles	Varied number of interfaces (Fig. 3 (f))	5.5 @ 600 K
TMDC hybrid	Ouyang *et al.* (2016) [147]	NEGF & MD & First-principles	Armchair MX_2 hybrid NRs (M = Mo/W, X = S/Se)	2-3 @ 300 K 7.4 @ 800 K

Note: Gr = graphene

3.1.2 Porous structures

Another important type of nanostructure is the porous structure where arrays of atomic- to nano-scale holes are introduced inside the 2D lattices. With tunable phonon transport and electron band structures, these 2D porous structures are named as antidot lattices, nanomeshes, or phononic structures [16],[148]. Several 2D porous structures have been theoretically investigated for thermal, electronic and thermoelectric properties, including the most studied graphene antidot lattices (GAL) [148]–[158], porous silicene [159], and 2D MoS_2 and phosphorene antidot lattices [160]–[161]. On the one hand, phonon transport in these porous structures can be significantly suppressed by boundary scattering and localization of phonons around the pores, as well as wave-like phonon interference in periodic structures [16],[152],[153]. On the other hand, the electronic band structure can be tailored in well-designed porous structures so that the Seebeck coefficient can be enhanced while the electrical conductivity can remain high [154]–[161]. Up to now, several theoretical studies have demonstrated enhanced *ZT* values in 2D porous structures, as listed in Table 2.

GALs with nanoscale pores have been extensively studied for the electronic properties [148]–[151], demonstrating a nonzero band gap around the nanopores. As for thermal transport, Yang and co-workers [152] demonstrated by MD simulations that the thermal conductivity of periodic graphene nanomeshes can be effectively tuned by changing the porosity and period, with the thermal conductivity reduced to 0.1 to 0.01 of that of pristine graphene as the porosity changed from ~21% to 65%. Feng and Ruan [153] studied thermal transport in graphene nanomeshes with 5 nm neck width, 10-20 nm pore sizes, and different pore shapes and arrangements using MD simulations. The thermal conductivity of the graphene nanomeshes was found to be 3 orders of magnitude lower than that of pristine graphene, and even 200-fold lower than that of GNRs with the same neck width, showing great potential for thermoelectric applications [153]. Further, several groups reported simultaneous simulations of phonon and electron transports in various graphene porous structures (or GALs), which yielded reduced thermal conductivity, maintained electrical conductivity, and enhanced Seebeck coefficients [154]–[158]. As listed in Table 2, the reported *ZT* values of GALs ranged from 0.2 to ~3. Especially, Chang and co-workers [158] modified the GAL by adding adatoms, which can enhance the spin-orbit coupling and thus convert bulk graphene into a topological insulator with a bandgap and robust helical edge states. While phonon transport was significantly suppressed

by the nanopores, the Seebeck coefficient reached up to 1 mV/K and the maximum *ZT* value was as high as ~3 at 40 K [158].

Besides graphene porous structures, Sadeghi and co-workers [159] reported enhanced thermoelectric performance of silicene antidot lattices (Fig. 4 (d)), with the Seebeck coefficient up to 500 μV/K and the *ZT* value as high as 3.5. Shao *at al.* [160] reported electronic properties of MoS_2 antidot lattices (Fig. 4 (f)) using first-principles calculations and found tunable bandgaps with the supercell sizes and the foreign atom adsorption. Cupo and co-workers [161] reported tunable band gaps of phosphorene antidot lattices (Fig. 4 (e)) both theoretically and experimentally. Their DFT calculations revealed that the bandgap scaling can be attributed to quantum confinement effects [161].

Table 2. *ZT* values reported in theoretical studies of 2D porous structures

Material	Reference	Calculation method	Structure features	Max. *ZT*
GAL	Gunst *et al.* (2011) [154]	Landauer theory	Hexagonal holes with varied sizes and edge chiralities	~0.3 @ 300 K
GAL	Karamitaheri et al. (2011) [155]	Landauer theory	Circular, rectangular, hexagonal, and triangular antidot shapes (Fig. 4 (c))	~0.2 @ 300 K
GAL	Yan *et al.* (2012) [156]	NEGF	1D antidot arrays (Fig. 4 (a))	~1.0 @ 300 K
GAL	Hossain *et al.* (2015) [157]	DFT & NEGF	Rectangular hole with varied sizes	~0.8 @ 300 K
GAL	Chang *et al.* (2014) [158]	First-principles	Both heavy adatoms and nanopores (Fig. 4 (b))	~3 @ 40 K
Porous silicene	Sadeghi *et al.* (2015) [159]	DFT	Varied doping and edge termination (Fig. 4 (d))	3.5 @ 300 K

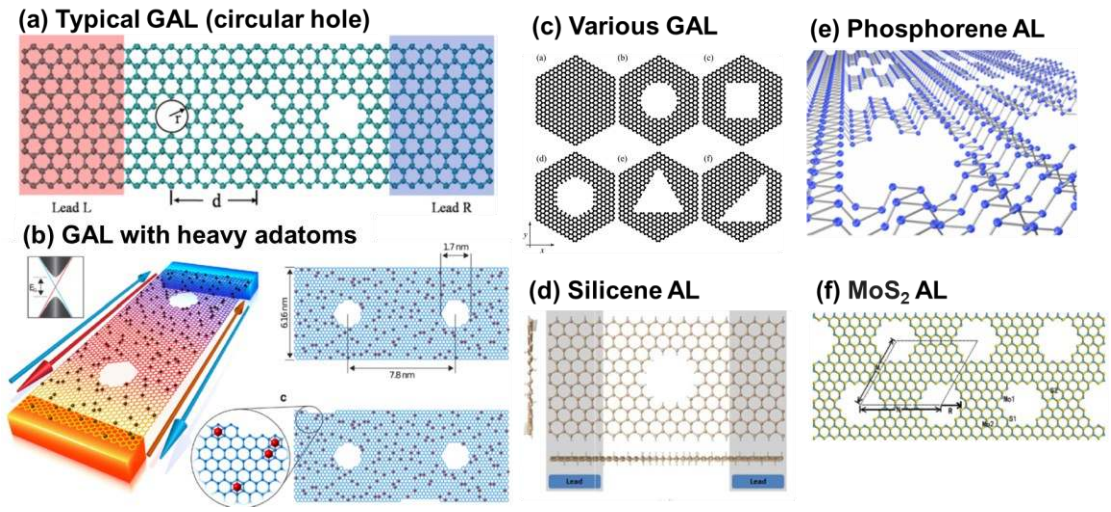

Fig. 4 2D porous structures. (a) Typical graphene antidot lattice (GAL) with circular holes (adapted from [156]). (b) GAL with heavy adatoms (adapted from [158]). (c) GAL with holes of different geometries (adapted from [155]). (d) Silicene antidot lattice (adapted from [159]). (e) Phosphorene antidot lattice (adapted from [161]). (f) MoS_2 antidot lattice (adapted from [160]).

3.1.3 Machine learning approaches

As suggested in the previous sections, there are infinite possibilities for the nanostructure patterns of 2D materials, and hence the case-by-case enumerative studies towards an optimized structure for thermoelectric applications are awfully expensive, inefficient, and often unsuccessful. To address this issue, the machine learning techniques or materials informatics have recently attracted growing interest in the field of thermal transport and thermoelectric studies [162]–[166]. Combining the limited data accumulated from simulations and experiments with the data-driven machine learning or AI approaches can greatly accelerate the discovery of high-performance thermoelectric structures. Especially, some machine learning algorithms have been utilized to optimize 2D nanostructures for the target properties. Yamawaki and co-workers [162] combined phonon and electron transport calculations of graphene nanostructures with Bayesian optimization, and successfully discovered certain structure configurations that can comprehensively optimize the thermal and electrical properties towards an enhanced thermoelectric figure of merit. Two kinds of well-defined graphene nanostructures were investigated for the optimization (Fig. 5): (1) the distribution of vacancy defects, and (2) one-dimensional configuration of the antidot lattice unit and pristine unit. The optimized antidot structure exhibited the highest *ZT* value that is 11 times that of the pristine GNR and more five times that achieved by random search, which was attributed to the zigzag edge states and the unique aperiodic nanostructure.

A recent work by Wei *et al.* [163] adopted a two-step search process coupled with the genetic algorithm to answer whether the thermal conductivity of GALs with periodically distributed holes is always higher than that of GALs with randomly distributed holes. Around these random holes, the phonon Anderson localization has been believed to largely suppress

phonon transport. Unexpectedly, Wei and co-workers discovered certain patterns of nanopore distributions with an enhanced thermal conductivity as compared to that of periodic pore distribution (Fig. 6), which was never found during the manual search. The unexpected thermal conductivity enhancement was attributed to the shape factor and channel factor in these unusual structures that dominate over the phonon localization. This study demonstrated the possibilities and complexity of the structure-property relationship in 2D nanostructures, which can stimulate further machine-learning based optimization and provide guidance for the rational design of two-dimensional structure patterns for enhanced thermoelectric performance.

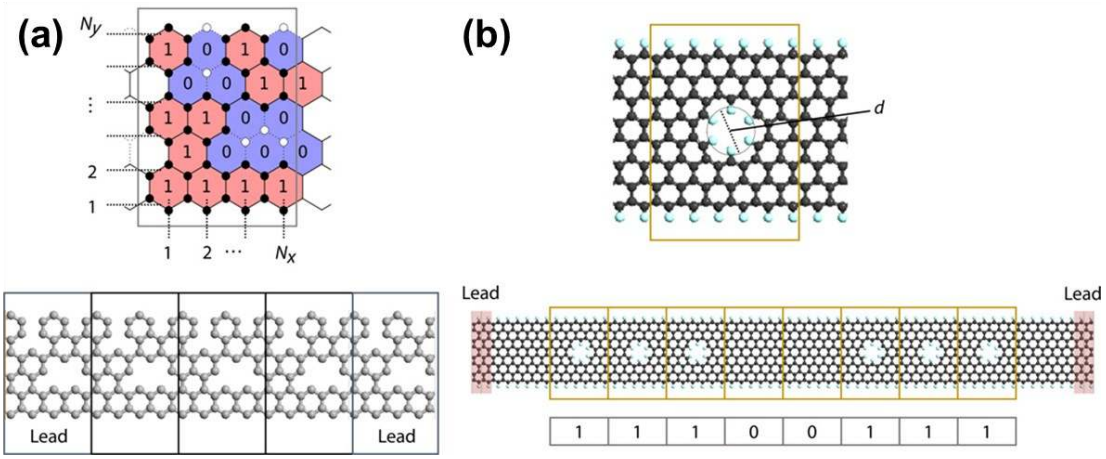

Fig. 5 Bayesian optimization for enhanced *ZT* of graphene nanostructures. (a) Optimization of the vacancy distribution (Model A). (b) Optimization of the arrangement of the pristine and antidot GNR cells (Model B). The descriptors, 0 and 1, respectively describe the defective and complete hexagonal lattices for Model A, and the pristine and antidot GNR cells for Model B. Adapted from [162].

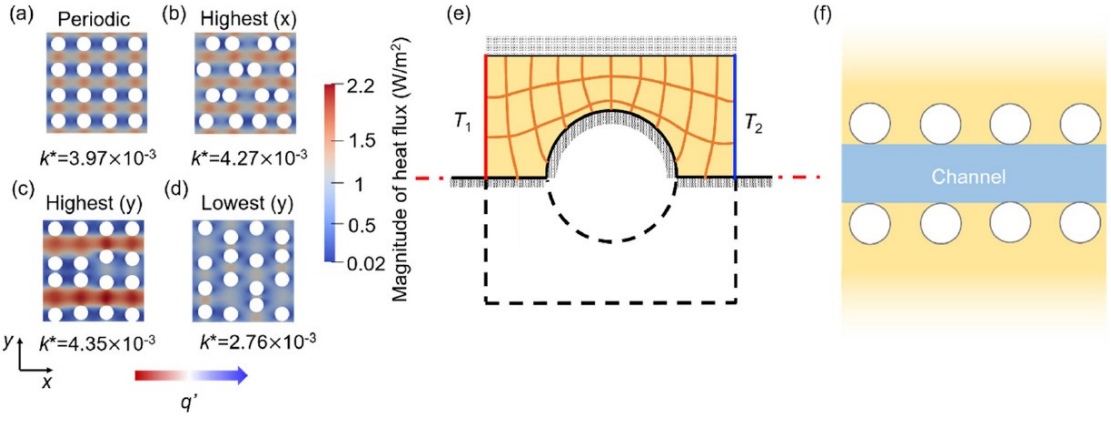

Fig. 6 Genetic algorithm (GA) driven discovery of thermal conductivity enhancement in disordered GALs. (a) Periodic configuration of nanopores, (b), (c) the configuration with the disorder in *x* and *y* direction identified by GA for high thermal conductivity, (d) the configuration with the disorder in *y*-direction identified by GA for low thermal

conductivity. (e) The shape factor illustrated using a quasi-1D heat conduction model. (f) Schematic of heat conduction channel. Adapted from [163].

3.2 Experimental progress

This section reviews the progress in experimental studies of nano-patterned 2D materials. Caution should be taken for the significant knowledge gap between computations in Section 3.1 and the experimental studies in this section. A few issues should be addressed:

1) Band structure computed by first-principles calculations [167]–[169],[149] (unit cell of ~100 atoms or less) or tight binding modeling [151],[170]–[174] (unit cell of ~10 nm sizes or less) often focus on pore diameters of ~1 nm or less. In addition, qualitatively estimate of the band structure can be obtained by fast numerical solutions of the Dirac equation [171]. In experiments, however, the smallest pore diameter is still in the sub-20 nm regime due to the restriction of employed nanofabrication techniques [175],[176].
2) The band gap opening is suggested to depend on the chirality of the supercell lattice vectors [168],[170], which has not been verified experimentally.
3) Structure disorder (e.g. irregular pore shape) [174],[172],[169], and the exact structure-edge configuration (i.e. armchair or zigzag edges) are considered in some computations but no atomic structure information from real samples is available for such studies.

Although electrical properties can usually be accurately measured, special attention should also be paid to the challenges of thermal measurements. As the most accurate approach for the thermal measurements of nanostructures, the thermal conductivity of a nanostructure can be obtained from steady-state and one-dimensioanl heat conduction along the structure. This can be achieved with suspended heater-thermometer membranes [177],[178] or metal lines [200] bridged by the measured nanostructure. For fragile nanoporous structures, this approach has not been used though it can be found for supported graphene nanoribbons [200] and suspended graphene [179],[180]. Metal deposition is often used to form good thermal/electrical contacts between the sample and the suspended device. Along another line, non-contact Raman thermometry can also be used to extract the in-plane thermal conductivity of a suspended 2D material. The model can be either based on a self-heated suspended strip [181] or laser-heated sample with circular temperature profiles from the laser spot [182],[183],[34],[202]. Besides the less accurate temperature reading of Raman thermometry, accurate thermal analysis may also involve the strong thermal nonequilibrium between electrons, optical phonons and acoustic phonons [183],[195] in laser-heated 2D materials.

Keeping these in mind, reliable and systemaic thermoelectric measurements should be carried out with more advanced nanofabrication techniques to control the patterns at the atomic level. Nevertheless, the experimental results in this section are still critical and some of the materials can be useful in applications already.

3.2.1 Porous structures

Despite many theoretical studies, extremely limited experiments have been carried out to demonstrate the predicted thermoelectric performance of 2D nanostructures due to the challenges of both sample fabrication and thermal measurements at the nanoscale.

The fabrication of 2D porous structures can be classified into three categories: (1) chemical etching or plasma treatment to introduce random and uncontrollable holes or defects [172],[191], (2) helium or gallium ion-beam based direct drilling of holes in the 2D material [189],[190], and (3) mask based patterning (electron beam lithography [161],[186], or block copolymer self-assembled porous mask [185]) followed by plasma etching processes. The electron beam lithography-based patterning can offer the most accurate and large-scale control of the nanostructure, with the smallest pore diameter around 15 nm [186]. The helium ion beam-based milling yielded the smallest pore size of approximately 6 nm in diameter [191].

Xiao and co-workers [172] treated few-layer graphene (FLG) with oxygen plasma for 10–20 seconds to introduce atomic scale holes (defects). The Seebeck coefficient of the plasma-treated few-layer graphene was measured to be as high as 700 μV/K at 575 K, which was attributed to the bandgap opening induced by the local holes or defects [172]. The electrical conducrtivity of the randomly etched FLG was ~10^4 S/m, which is 2 orders of magnitude lower than high-quality samples, and the *PF* was 4.5 mW/m·K^2, only about half that of high-quality pristine graphene. Such plasma treatment can not be used for single-layer graphene that can be easily destroyed by plasma ecting [172]. Similar random chemical etching was recently adopted by Kang et al. [191] to introduce random holes in 7 nm-thick MoS_2 thin films, the in-plane Seebeck coefficient of which was measured to be up to ~742 μV/K.

Using the block copolymer self-assembly method (Fig. 7), Oh and co-workers [185] fabricated mono- and bi-layer graphene nanomeshes with irregular holes. The hole diameter in the nanomeshes was about 20–40 nm, and the average neck widths were 8–21 nm. They measured the Seebeck coefficient and electrical conductivity of SiO_2-supported samples by a commercial instrument (TEP-600, Seepel Instrument, Korea), and measured the effective thermal conductivity of a different suspended porous graphene sample by the Raman optothermal method. Note that the Raman-based measurement here can involve large uncertainties due to several factors, including the unknown laser absorption and phonon nonequilibrium as well as the relatively low sensitivity for temperature detection [192]–[195], which we will discuss in more detail later. The bilayer graphene nanomesh with 8 nm neck width exhibited the lowest thermal conductivity of about 78 W/mK around 350 K due to the phonon scattering at the neck edge, and the highest Seebeck coefficient of -190 ± 80 μV/K at 300 K and −520 ± 92 μV/K at 520 K, which can be explained by the bandgap opening. However, the electrical conductivity was significantly reduced by 2 orders of magnitude to be around 2 $\times 10^4$ S/m, which should be originated from the defects and contamination introduced in the nanofabrication processes. Oh and co-workers achieved a *PF* of about 8.2 mW/m·K^2 at 520 K in the bilayer nanomesh with 8 nm neck width due to the superior Seebeck coefficient, but the *ZT* of all the measured nanostructures were even decreased by 1–2 orders of magnitude as compared to large-area graphene because the electrical conductivity was not maintained high enough.

Although this work provided the first experimentally measured *ZT* for GALs, the thermal contact between the sample and the thermal probes may largely affect Seebeck coefficient measurements, where the measured temperatue difference can be larger than that "felt" by the sample. Some *PF*s given by Oh and co-workers [185] were suspected to be an underestimate of the actual values. On the other hand, their thermal measurements used a Raman laser as a heat source and read the temperature from the Raman peak shift. The laser light was focused on a GAL suspended across a membrane hole. The laser spot acted as a heating source, whereas the membrane was the heat sink to "drain" the heat from the suspended sample. The effective thermal conductivity of a GAL was thus obtained from 2D heat conduction analysis. One challenge was how to determine the actual laser power absorbed by a sample. In the work by Oh *et al.*, the possible light reflection by the graphene antidot lattice was neglected and the laser power not transmitted through a sample was considered to be absorbed. In addition, the in-air measurements were affected by convection and air conduction around the sample, which was usually hard to be estimated. More accurate measurements also required a better understanding of light absorption by graphene, i.e., the strong thermal nonequilibrium between electrons, optical phonons and acoustic phonons [183],[195].

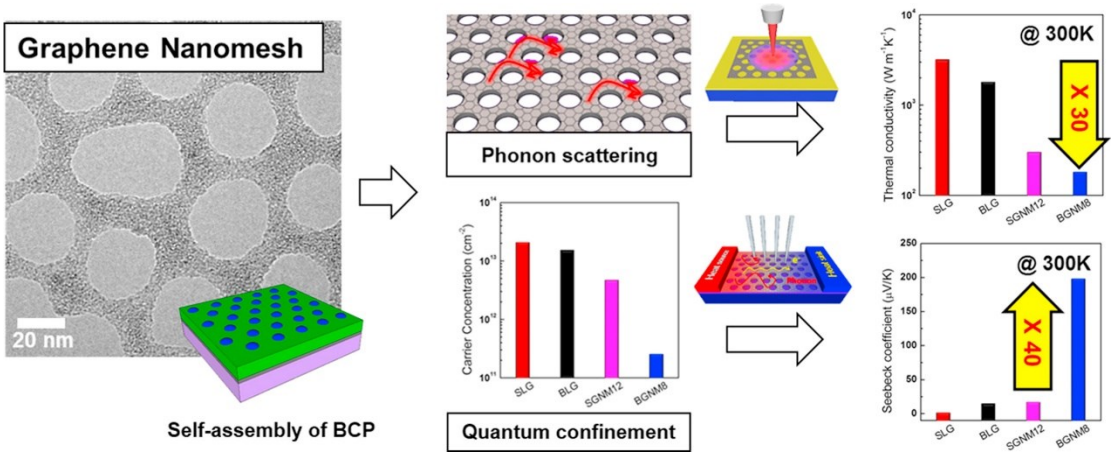

Fig. 7 Reduced thermal conductivity and enhanced Seebeck coefficient measured in graphene nanomeshes. Adapted from [185].

Xu and co-workers [186] fabricated GALs by the electron beam lithography and reactive ion etching. To minimize the measurement errors, deposited metallic electrical/thermal probes were used to ensure good thermal/electrical contacts. The square and hexagonal patterns were compared for their electrical properties. The square pattern exceeded the hexagonal pattern for the *PF* under an gate voltage that maximized $|S|$ (Fig. 8 (c)). At 400 K, a remarkable *PF* of 554 $\mu W/cm \cdot K^2$ is achieved in the p-type GAL with a square pattern, which is far beyond the best *PF*s of bulk thermoelectric materials. One innovation of this work was to better analyze the maximum Seebeck coefficient under an applied gate voltage, from which the carriers' energy sensitivity (j) to scattering (CEStS) was extracted to better understand the scattering mechanisms of charge carriers. In physics, this CEStS is defined as $j = d\left[\ln(\tau)\right] / d\left[\ln \varepsilon\right]$, where τ is energy-depdent relaxation time, ε is the carrier's energy referring to the edge of

the corresponding valley. The extracted j in Fig. 8 (d) reflects a statistical measure of the average values of j for all existing scattering mechanisms. Because the divergence between electrons and holes is within 10%, the averaged j value is plotted here. Here the positive j value indicates increased importance of the long-range scattering sources at elevated temperatues. This new technique can be applied to general 2D materials for better understand their electron transport processes.

Due to the experimental complexity, the pore-edge configuration (e.g. armchair or zigzag) was not checked in all measured samples. The pore sizes are also significantly larger than those used in computations. In this aspect, high-quality samples may be prepared by the direct growth of a nanoporous pattern with SiO_2 pillar as the mask that can be removed with hydrofluoric acid etching later. A similar study can be found for the direct growth of nanoporous $In_{0.1}Ga_{0.9}N$ films for thermal studies [187]. A more perfect structure, with an ordered inclusion of uniform holes and nitrogen atoms, can be directly synthesized. Examples can be found in C_2N-h2D crystals [239], polyaniline (C_3N) with six nitrogen atoms periodically surrounding a phenyl ring [240]. Phonon studies are also carried out on monolayer C_3N structure with a periodic array of zigzag holes [188].

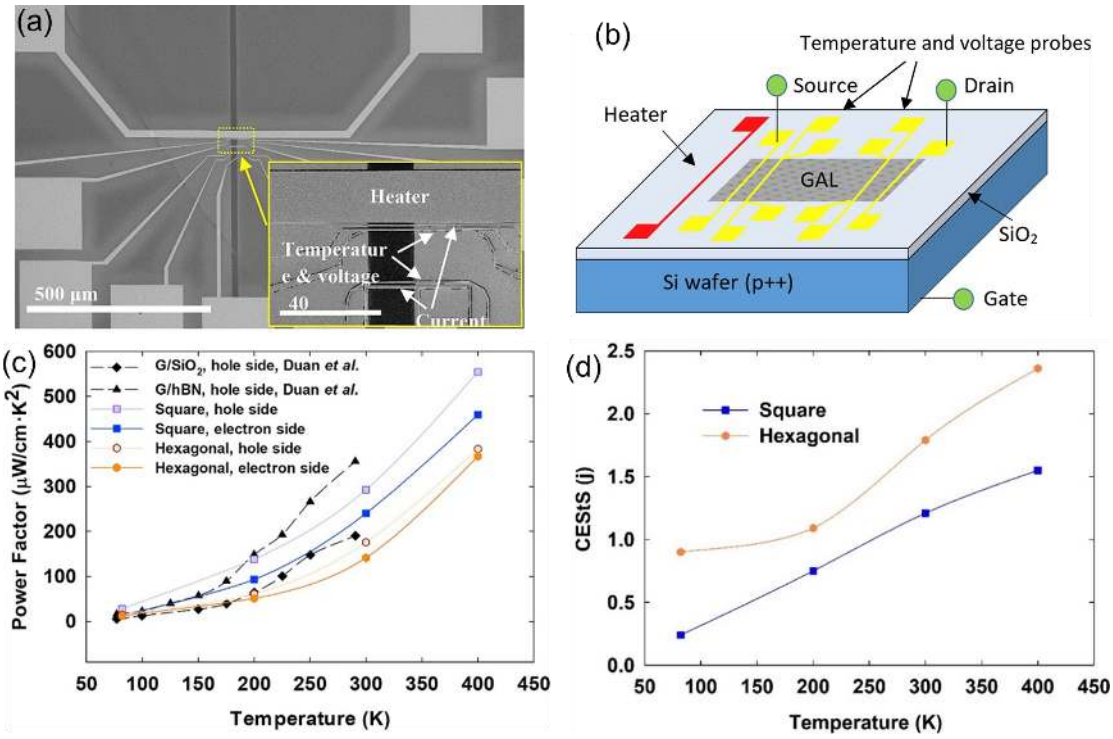

Fig. 8 The enhanced *PF* of GALs and the detection of major charge-carrier scattering mechanism. (a) SEM image of the test device. (b) Schematic of the measurement principles. (c) *PF*s of different samples as a function of temperature. (d) The CEStS (j) of GALs with a square array and a hexagonal array of nanopores. Adapted from [186].

3.2.2 Graphene nanoribbons

Han and co-workers [199] first experimentally demonstrated the bandgap opening in lithographically patterned GNRs in 2007. The bandgap increased from 3 meV to 300 meV as the GNR width decreased from 90 nm to 15 nm [199], thus we can expect an enhanced Seebeck coefficient in GNRs with a width of several tens of nanometers. Recent experimental progress has also confirmed drastic reduction of thermal conductivity in both SiO_2-supported and suspended GNRs (Fig. 9). Bae and co-workers [200] patterned exfoliated graphene sheets into arrays of GNRs with ~260nm length and 45−130 nm widths using electron beam lithography and deposited the hearer and sensor on top for the thermal conductivity measurement of SiO_2-supported GNRs (Fig. 9 (a)). The thermal conductivity exhibited a clear width dependence that scales as $k \sim W^{1.8\pm0.3}$, with the room-temperature k of 65-nm-wide supported GNRs suppressed to about 100 W/mK, about one-sixth of large-area supported graphene [10]. This reduction of k was mainly attributed to the strong scattering between phonons and the plasma-etched rough ribbon edges. Also using the lithographical patterning and plasma etching followed by substrate etching, Li and co-workers [197] measured the thermal and electrical conductivities of an individual suspended GNR with 169 nm width and 846 nm length (Fig. 9 (b)). The RT thermal and electrical conductivities of the 169-nm-wide suspended GNR were about 350 W/m·K and 9×10^5 S/m, respectively. This thermal conductivity was about 15% of that of large-area suspended graphene, which can be explained by phonon-edge scattering, but the electrical conductivity was also largely reduced as compared to pristine graphene because of the inevitable defects and contaminations from the lithographical processes. The ZT value of this sample could be estimated to be on the order of 10^{-3} by assuming the Seebeck coefficient the same as that of large-area graphene. Later, using MEMS fabricated metallic heater and sensors, Hossain and co-workers [198] measured the Seebeck coefficient of graphene sheets and a patterned individual 50-nm-wide GNR supported on SiO_2. The Seebeck coefficient was measured to be enhanced from ~10 μV/K for the graphene sheet to ~30 μV/K for the GNR, which demonstrated the nanostructure effect on the Seebeck coefficient although both were quite low values due to the sample quality.

A recent work by Li *et al.* [196] finally realized the enhancement of ZT of graphene by several orders of magnitude (Fig. 9 (c)). Li and co-workers [196] designed a one-process approach to fabricate suspended high-quality GNRs along with an 8-terminal test device. Instead of lithographical patterning, the suspended GNRs were directly synthesized by a method called plasma chemical vapor deposition. In this synthesis method, a nanoscale Ni thin film bridging the Ni heater and sensor acted as the catalyst and melted during the synthesis, leaving the above GNR free-standing. The as-grown process ensured a low number of defects and relatively smooth GNR edges, which is important for maintaining high electrical conductivity. The 8-terminal device allowed simultaneous measurements of thermal and electrical conductivities and the Seebeck coefficient. The 40-nm-wide and ~250-nm-long samples exhibited record-high ratios of electrical conductivity to thermal conductivity for graphene that were 1-2 orders of magnitude higher than those previously reported. Detailed phonon BTE simulations revealed that the reduction of thermal conductivity mainly resulted from quasi-ballistic phonon transport, and the significant enhancement of σ/k is attributed to disparate electron and phonon MFPs and the defect-free samples. Furthermore, the Seebeck

coefficient was 87.7–125.7 μV/K at 80–220 K, several times that of large-area graphene because of bandgap opening. As a result, the *ZT* reached record-high values for graphene of about 0.1, which demonstrated that nanostructured graphene can be a superior thermoelectric material for power generation as predicted in the theoretical studies.

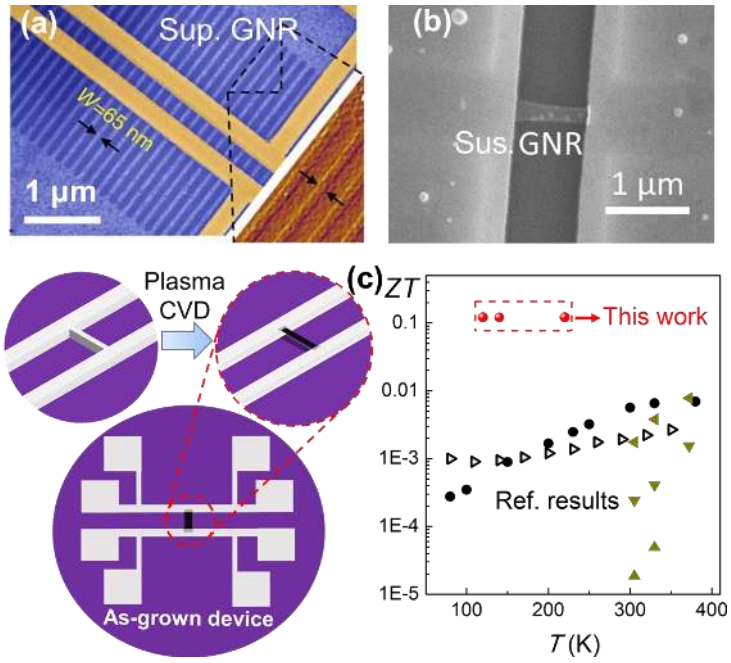

Fig. 9 Thermal and thermoelectric measurements of graphene nanoribbons (GNRs). (a) Thermal conductivity measurements of SiO_2-supported GNRs (adapted from [200]). (b) Thermal conductivity measurements of suspended GNRs (adapted from [197]). (c) Record-high *ZT* measured in as-grown 40-nm-wide suspended GNRs (adapted from [196]).

4. Van der Waals heterostructures for thermoelectrics

One of the advantages of 2D materials is the ability to tune their bandgap, hence tuning the thermoelectric *PF*. The change in the bandgap could be achieved by changing the number of layers, applying strain or electric field, and changing the structural composition of the material (by hydrogenation or oxidation). For example, by reducing the number of layers of arsenic from its semimetallic bulk, one can observe a transition to a semiconducting state. The monolayer honeycomb structures of arsenic, called arsenide, is a semiconductor with an indirect bandgap of 0.831 eV.[201] The electronic transport of 2D layers also depends on the type of substrate used. Via long-range Coulomb interaction, the impurities in the substrate can affect the electrons moving in the 2D layer material. The lattice constant mismatch between the substrate and the 2D layer can cause strain/stress on the 2D material and modify its electronic structure. The mismatch of the crystal structure can result in breaking the symmetry and also can modify the electronic structure of the 2D layer. In the first part of this section, we focus on

the in-plane thermoelectric transport with the substrate and the number of layers as two important parameters in mind.

The discovery of 2D layered materials and the possibility of mixing and matching atomically thin layers by stacking them on top of each other, open up a new exciting opportunity. Millions of combination of the different 2D layers with different band structures are now possible to engineer the energy potential of electronic transport, enabling the design of high-*PF* structures. At the same time, due to the nature of the weak van der Waals bonds, these 2D layered materials, inherently own very low thermal conductivity values in the cross-plane direction and hence pave the way for the design of solid-state thermionic structures. In the second part of this section, we focus on the cross-plane thermoelectric transport in 2D layered structures with less than 10 layers.

4.1 In-plane transport

The transport properties of 2D layers are a strong function of the substrate that they are placed on. In section 2, we focused on the thermoelectric properties of 2D layers placed on SiO_2/Si substrate which is the most widely used substrate. Here, we summarize some of the results obtained by using a different substrate or placing on hBN or graphene in between the 2D material and the SiO_2 substrate.

Duan and co-workers [5] fabricated graphene on hBN samples using the poly(methyl methacrylate) (PMMA)-based dry transfer method, and patterned metallic heater and thermometers on top the heterostructure for the electrical conductivity and Seebeck coefficient measurements. They found that the Seebeck coefficient of graphene on hBN can be twice that of graphene on SiO_2, and meausured the room-temperature *PFT* value of the graphene/hBN device up to 10.35 W/mK (Fig. 10 (c)), which exceeded all the previously reported room-temperature *PFT* values for both 3D and 2D materials. Duan *et al.* [5] further demonstrated that the Seebeck coefficient offers a measure of the substrate-induced random potential fluctuations and the hBN substrates can enable larger bipolar switching slopes for the Seebeck coefficient (Fig. 10 (b) and (d)). Combining the high *PF* with the large thermal conductivity of both graphene and boron nitride, this work by Duan and co-workers demonstrated that the graphene/hBN heterostructure can be a very promising material for active cooling of electronics. Wu and co-workers [213] fabricated MoS_2/hBN heterostructure samples with sulfur vacancies and measured the in-plane thermoelectric properties using a similar approach as in Ref. [5]. The n-type MoS_2 on hBN exhibited an extremely large positive Seebeck coefficient of 2 mV/K in the on-state because of the magnetically induced Kondo effect [213]. Further, by tuning the chemical potential, Wu *et al.* measured a *PF* as high as 50 $mW/m \cdot K^2$ at 30K or *PFT* value of 1.5 W/mK.

By combining the nanostructuring and stacking approaches, Oh and co-workers [208] fabricated sub-20 nm GNR arrays on monolayer MoS_2. They measured the in-plane electrical conductivity and Seebeck coefficient of the GNR/MoS_2 heterostructure using a commercial instrument and achieved a relatively high *PF* of 222 $\mu W/mK^2$ [208].

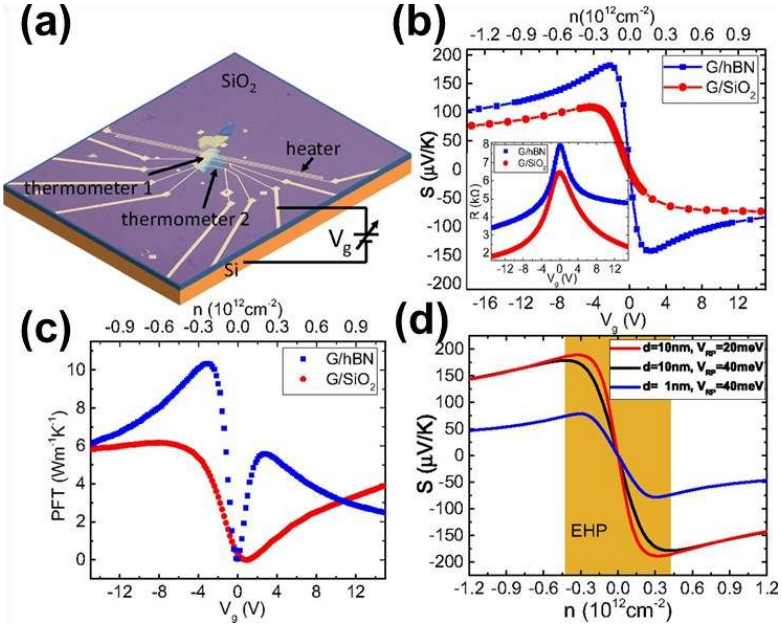

Fig. 10 A graphene/hBN heterostructure device with an enhanced in-plane *PF*. (a) Schematic of the thermoelectric measurement device. (b) Seebeck coefficients as a function of the gate voltage for G/hBN and G/SiO_2 at 290 K. (c) *PFT* as a function of the gate voltage for G/hBN and G/SiO_2 at 290 K. (d) Simulation of the Seebeck coefficient as a function of the carrier density at 300 K, with different hBN thicknesses, *d*, and random potential fluctuations, V_{RP}. Adapted from [5].

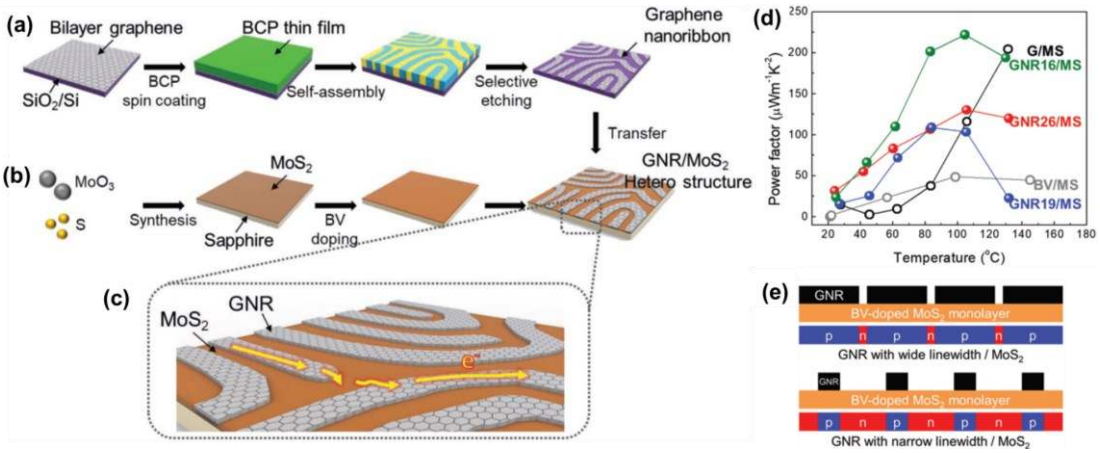

Fig. 11 GNR/MoS_2 heterostructures with improved thermoelectric properties. (a) Fabrication of the GNR network. (b) Synthesis of doped MoS_2. (c) Schematic diagram of the in-plane carrier movement across the GNR/MoS_2 van der Waals heterojunctions. (d) The *PF*s of the GNR/MoS_2 heterostructures. (e) Schematic images of the GNR/MoS_2 heterostructures with wide and narrow GNRs. Adapted from [208].

A very interesting recent work ([94], Fig. 12) shows that the thermoelectric *PF* of FeSe films, a high-T_c superconductor, placed on $SrTiO_3$ substrate increases as the thickness decreases.

When the films are about 1-nm thick, the equivalent of a bilayer, the thermoelectric *PF* increases to values as large as 1.30 W/m·K^2 or *PFT* value of 390 W/m·K. [94] This value is larger than anything reported before especially at such a low temperature. This large enhancement is attributed to the strong electronic correlation of FeSe electrons. Other possibilities such as the effect of the substrate, the ionic liquid used for gating, and the phonon drag effect are disputed by the authors but require more through theoretical insights. As mentioned in section 2, similar thickness dependence has been observed for MoS_2 placed on SiO_2 and 2L MoS_2 possesses the best *PF* [12],[49].

Other than a single graphene sample, a counterflow room-temperature *PF* of ~700 $\mu W/cm \cdot K^2$ was reported for bilayer-graphene double layers separated by a thin (~ 20 nm) boron nitride layer (Fig. 13), where top and bottom gate voltages are separately applied to each graphene layer [222].

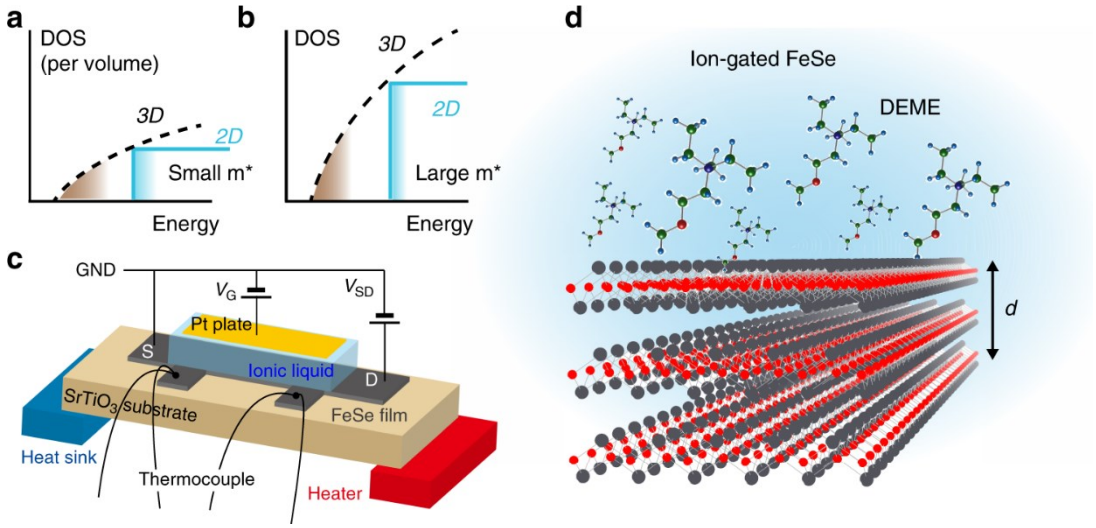

Fig. 12 Thermoelectric measurement of ion-gated FeSe thin films. (a) Schematic illustration of the DOS for 3D and 2D electrons. (b) The large effective mass *m enhances the DOS, which is beneficial for enhancing the Seebeck effect. (c) Device structure for thermoelectric measurement. (d) Enlarged illustration of the ionic liquid/FeSe interface. Adapted from [94].**

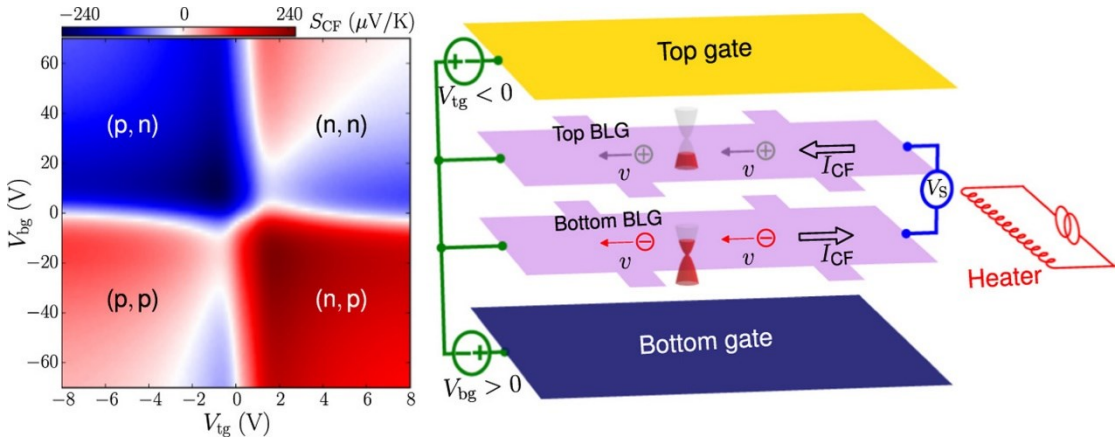

Fig. 13 A graphene/hBN heterostructure device with an enhanced in-plane *PF*. (a) Schematic of the thermoelectric measurement device. (b) Seebeck coefficients as a function of the gate voltage for G/hBN and G/SiO_2 at 290 K. (c) *PFT* as a function of the gate voltage for G/hBN and G/SiO_2 at 290 K. (d) Simulation of the Seebeck coefficient as a function of the carrier density at 300 K, with different hBN thicknesses, *d*, and random potential fluctuations, V_{RP}. Adapted from [222].

4.2 Cross-plane transport: solid-state thermionic structure

Here, we focus on 2D layered materials with metallic contacts on the top and the bottom and hence transport of electrons and phonons perpendicular to layer planes wherein an energy barrier is formed due to the band alignment of the heterostructure. When there is only a monolayer, transport is dominated by electron tunneling. Due to the transfer of low energy electrons, expected *ZT* values of tunneling interfaces is small. The tunneling can be eliminated by increasing the number of layers. It is shown that about 4 layers are needed to suppress the tunneling effects [223] and force the electrons to go above the energy barrier, the so-called thermionic transport is then dominant. The concept of solid-state thermionic cooling was first proposed by Shakouri [224] and later evaluated both in the power generation and the cooling mode by Mahan [225]. These structures are in between vacuum state thermionic generators and thermoelectric generators. Similar to vacuum state thermionic generators [226]–[229], there is an energy barrier that electrons need to overcome to move from the hot cathode to the cold anode. The energy barrier of a vacuum state thermionic generators is determined by the work-function of the metallic cathode and anode. Since the work function of metals is on the order of eV, temperatures larger than 1000 K are needed for electron transport. This problem is resolved in solid-state thermionic generators since the energy barrier can be adjusted to much lower values by proper choice of the metal-semiconductor interface. In these structures, the difference between the metal work function and the electron affinity of the semiconducting layer determines the electronic energy barrier. Hence by designing the energy barrier to few k_BT, one can design the appropriate generator for the given operating temperature, T. In the case of 5 to 10 layers of 2D van der Waals heterostructure, the chemical potential is pinned by the metallic contact but the energy barrier can be engineered with a high degree of flexibility by finding the right sequence of layers [230],[231].

When the thickness of the 2D layered material is comparable or larger than the electron MFP, we see a transition from ballistic transport to diffusive transport which is closer to thermoelectric transport. In this case, transport is mostly a function of the semiconducting layers and the effect of the contacts is minimum and limited to the electrical and thermal contact resistances at the metallic interfaces. The situation is different in solid-state thermionic generators. There, due to the ballistic nature of transport, electrons are not in near equilibrium with the lattice of the semiconducting layer. Hence, to understand thermionic transport, metallic contacts need to be included in the analysis. The combination of cathode-semiconductor-anode determines the energy barrier, the positioning of the chemical potential, and hence the thermionic *PF*.

Several theoretical works have shown the potential of 2D van der Waals heterostructures for solid-state thermionic applications and they all point to large *ZT* values. [223], [232]–[234] However, all calculations are done for ideal interfaces. In practice, making such ideal clean interfaces using transfer techniques is not realistic. Hence, the future of this field should be guided by more experimental results.

In the out-of-plane direction, one of the experimental challenges is how to determine the temperature gradient across the atomic thin layers for the thermal and thermoelectric characterization. The Raman spectroscopy based non-contact thermometer enables simultaneous temperature detection of every atomic thin material from their distinct Raman peaks that shift with temperatures [34],[192],[193],[221], and thus has been employed to measure the thermal boundary resistance at the van der Waals interface and the Seebeck coefficient in the cross-plane direction. Chen and co-workers [207] stacked graphene on the insulating hBN and patterned electrodes on graphene to provide Joule self-heating. The Joule heat flux transferred across the heterojunction and the temperatures of both the graphene and hBN layers were simultaneously measured from the Raman spectrum (Fig. 14 (a)), from which the thermal boundary conductance (TBC) between graphene and hBN was determined to be 7.4 MW/m^2K. Vaziri *et al.* [203] applied this technique of combining Joule heating and Raman thermometry to the thermal measurement of more complicated heterostructure devices involving graphene (Gr), MoS_2, and WSe_2 (Fig. 14 (c)). The TBC values at the 2D/2D interfaces were measured to be 5 ± 3 MW/m^2K, 10 ± 3 MW/m^2K, and 9 ± 3 MW/m^2K for the Gr/WSe_2, Gr/MoS_2, and MoS_2/WSe_2 interfaces, respectively, which were significantly lower than those at the 2D/3D(SiO_2) interfaces (Fig. 14 (d)). Besides, Li *et al.* [202] combined laser heating and Raman thermometry, and developed a variable-spot-size transient Raman opto-thermal method to measure both in-plane and cross-plane thermal properties of 2D heterostructures in a non-contact manner (Fig. 14 (b)).

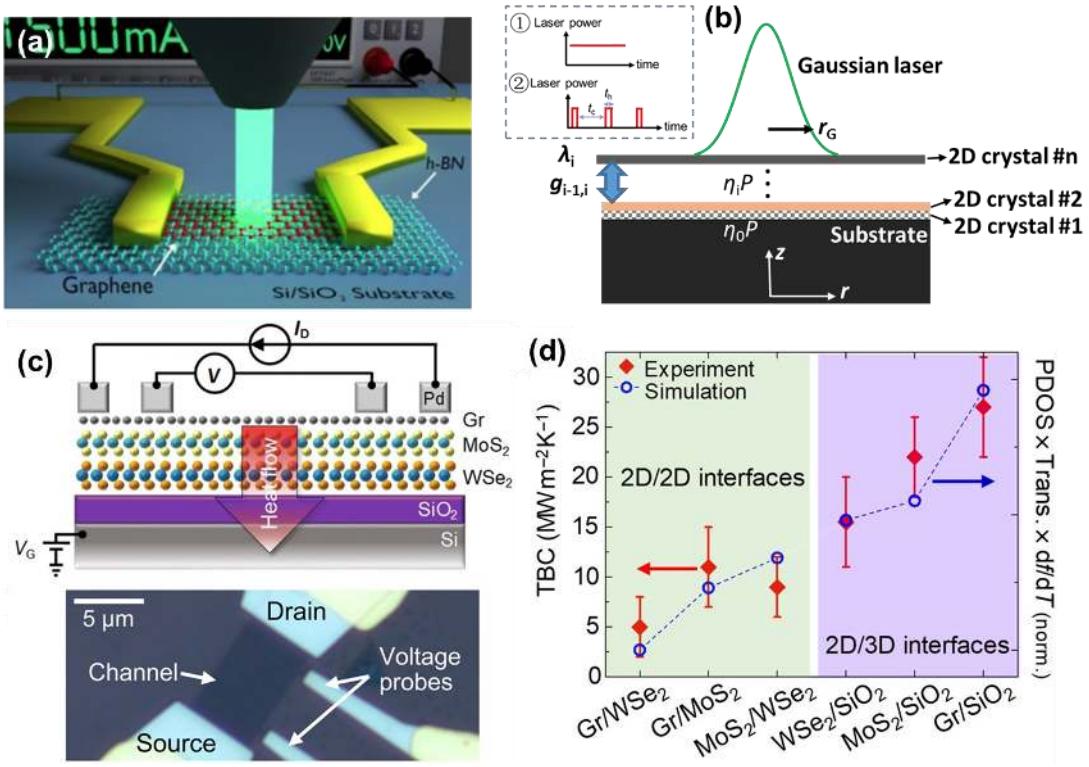

Fig. 14 Raman thermometry based thermal transport measurements of 2D van der Waals heterostructures. (a) Measurement of TBC between graphene and hBN using the Joule-heating and Raman-thermometer method (adapted from [207]). (b) The variable-spot-size transient Raman optothermal method to measure the in-plane and cross-plane thermal properties of van der Waals heterostructures (adapted from [202]). (c) Measurement of TBC between multilayer heterostructures using the Joule-heating and Raman-thermometer method. (d) Measured room-temperature TBC values of 2D/2D and 2D/3D (with SiO_2) interfaces and the calculated product of phonon DOS, phonon transmission, and d*f*/d*T*, normalized to the minimum achieved for Gr/WSe_2. (c) and (d) are adapted from [203].

Another widely studied technique for thermal boundary resistance measurement is the time domain thermo-reflectance method (TDTR). [235] TDTR has been widely used to measure the thermal transport across various interfaces. However, only recently this method is extended to small scales enabling measurement of micron-size flakes. In the context of cross-plane thermoelectric transport measurements, TDTR is recently used to measure thermal conductance across Au/Ti (or TiOx)/WSe_2/HOPG. It is shown that the TBC depends on the details of the contact, and the level of oxidization of titanium and is in the range of 6 to 22 MW/m^{2}K. Despite the small thermal conductance values, the studied interface has a low *ZT* due to the dominance of the electronic tunneling transport. [236]

A few experiments have been conducted to measure the cross-plane Seebeck coefficient of 2D heterostructures. Chen *et al.* [204] stacked a Gr/hBN/Gr heterostructure as shown in Fig. 15 (a), and patterned electrodes on the top and bottom graphene sheets. The top graphene was

fed with AC current to provide Joule heating and establish a temperature gradient in the cross-plane direction. The Seebeck voltage across the top and bottom graphene was measured from the 2ω voltage using the lock-in technique, while the temperature difference was detected by the Raman thermometry. In this way, Chen *et al.* comprehensively measured the thermal conductance, Seebeck coefficient, as well as the electrical conductance in the cross-plane for the same heterostructure device. The cross-plane Seebeck coefficient was –99.3 μV/K, the *PF* (S^2G) was 1.51×10^{-15} W/K^2, and the *ZT* was 1.05×10^{-6} for the Gr/hBN/Gr heterostructure. The extremely low *ZT* is the result of the low electrical conductance which in turn is due to the large energy barrier formed by the insulating hBN layer. Poudel and co-workers [206] reported a modified test device where the insulating Al_2O_3 and an indium tin oxide (ITO) transparent heater were coated on the Gr/hBN/Au heterostructure (Fig. 15 (b)). Similar with the work by Chen *et al.*, while the transparent top heater was driven with AC current to provide heat flux in the cross-plane direction, the temperature difference between graphene and hBN was measured from their Raman peaks and the cross-plane Seebeck coefficient was detected from the lock-in 2ω voltage, which yielded an interfacial Seebeck coefficient of −215 μV/K. Mahapatra and co-workers [205] stacked two layers of graphene sheets encapsulated by hBN using the layer-by-layer mechanical transfer method, as illustrated in Fig. 15 (c). The top graphene was conducted with AC current and the Seebeck coefficient across the twisted bilayer graphene was measured by the lock-in technique, while the temperatures of the two monolayers were determined from the temperature dependence of the in-plane electrical resistance of each graphene sheet. The maximum Seebeck coefficient of the van der Waals junction between graphene layers was measured to be 20−25 μV/K at a carrier density of 1×10^{11} cm^{-2} at ~70 K.

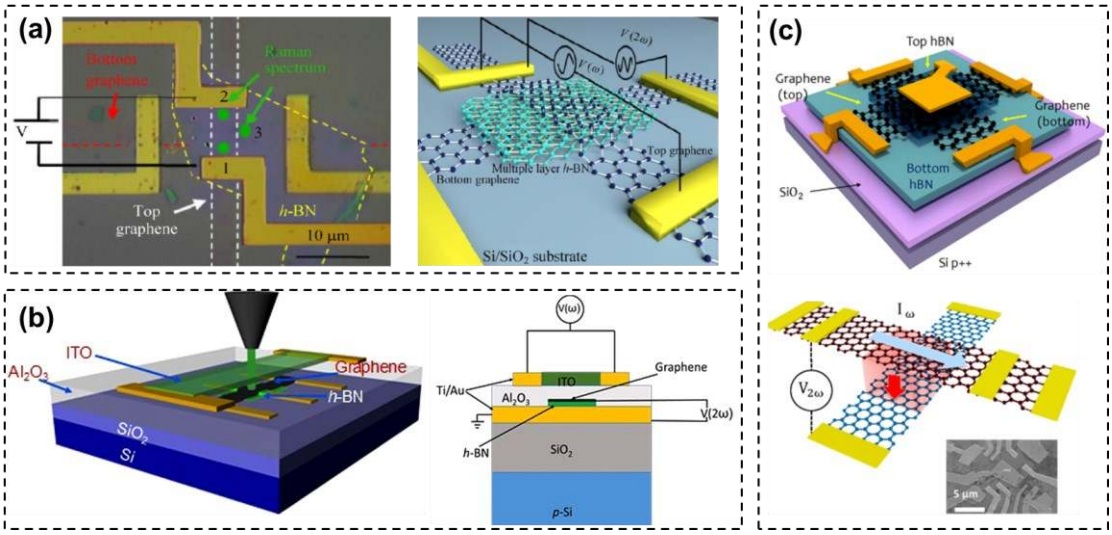

Fig. 15 Cross-plane Seebeck coefficient measurements of 2D van der Waals heterostructures. (a) Measurement of cross-plane Seebeck coefficient of a graphene/hBN/graphene heterostructure using Raman thermometry (adapted from [204]). (b) Measurement of cross-plane Seebeck coefficient of graphene/hBN/Au heterostructures using Raman thermometry (adapted from [206]). (c) Measurement of Seebeck coefficient across the van der Waals junction in bilayer graphene (adapted from [205]).

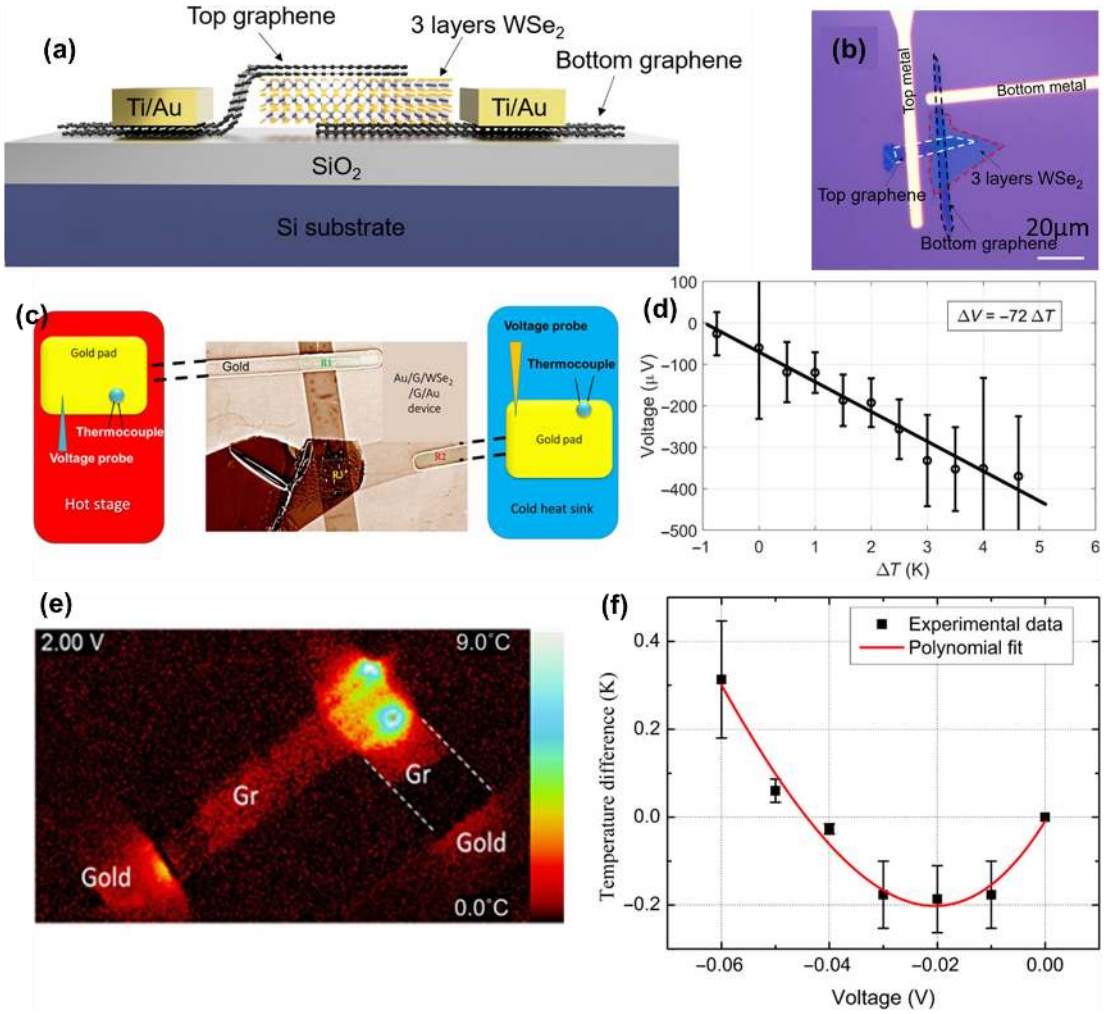

Fig. 16 Thermionic transport measurement across gold/Gr/WSe_2 van der Waals heterostructures. (a) Illustration of the cross-section of the Au/Gr/WSe_2/Gr/Au structure. (b) Optical microscope image of an Au/Gr/WSe_2/Gr/Au device. (c) Schematic of the Seebeck measurement setup. (d) Seebeck voltage measured versus applied temperature difference. (e) Joule heating: 2D temperature map of the Au/Gr/WSe_2/Gr/Au device under a relatively high-voltage 2 V obtained using the thermoreflectance method. (f) Cooling curve: Temperature difference between the substrate and top of the active device in Kelvin versus applied voltage at small applied voltages. Adapted from [237].

Rosul *et al.* [237] used a combination of TDTR measurements for determining the thermal conductance, the thermo-reflectance method for cooling curve measurements, and direct Seebeck measurement using thermocouples to study Au/Gr/WSe_2/Gr/Au structures (Fig. 16). They estimated a *ZT* value of 10^{-3} at RT which is the largest reported for nanometer-size thermionic structures. This small *ZT* is close to the predicted *ZT* using first-principles calculations and at RT for this structure. Theoretically, it is predicted that the *ZT* can be significantly improved by increasing the operating temperature and by changing the electrodes

from gold to platinum with a lower formed energy barrier. Hence developing the transport measurement techniques enabling high-temperature measurements, and developing techniques for more flexible fabrication of a variety of different metals-2D layers with clean interfaces, seems to be the most immediate need for further development of the 2D van der Waals based thermionic generators.

5. Summary and outlook

Instead of search for new materials, existing 2D materials can be tailored for their transport, optical, magnetic and other properties simply by patterned nanostructrues and stacked forms. Tremendous research opportunities exist in device- and energy-related applications. However, there is still many important issues to be addressed. First, accurate thermoelectric measurements for such fragile samples are still challenging and caution should be taken for the electrical/thermal contacts to the samples. For *ZT* calculations, the same sample must be measured along the same direction for all three thermoelectric properties. This can be more difficult in some cases and an integrated measurement setup is required to simultanesouly measure all properties, as demonstrated for nanoporous Si thin films [238]. Second, theoretical calculations often suggested the impact of detailed atomic structures, e.g., structure disorder, chirality, zigzag or armchair edges. This has been largely neglected in measurements. A unified picture is still missing here. In addition, the disconnection between theoretical studies and experimental measurements can also be found in the structure dimension, where ultrafine nanoporous 2D materials are still hard to be fabricated. In this aspect, directly grown 2D porous materials with uniform sub-1 nm holes [239],[240] may allow direct comparison between theoretical and experimental studies. High-energy electron or ion beam can also be used to drill sub-1 nm pores but attention should be paid to the atomic structure around pores [241]–[243]. Third, more advancements are required in first-principles predictions of the transport properties. For materials genome, a high-throughput calculation method is required and this can be achieved with machine learning. Successful examples for machine learning in materials search and design can be found for interfacial thermal conductance [165],[244],[245], bandgap [246], and interatomic force constants [247],[248],[249] used in MD simulations. Machine learning driven by experimental data is desired for thermoelectric studies, but is still lacking due to the challenge of high-throughput measurements at the nanoscale. Finally, the device-level applications of these materials and their mass production should receive more attention. The high nanofabrication cost of some nanostructured or stacked 2D materials may hinder their wide applications.

Acknowledgments

This work was partially supported by JSPS KAKENHI (Grant No. JP20H02090) and the JST CREST Grant Number JPMJCR18I1, Japan. Hao acknowledges the support from NSF (grant number CBET-1803931). Zebarjadi acknowledges the support from NSF grant number 1653268.

References

[1] Dollfus, P., Nguyen, V. H., & Saint-Martin, J. (2015). Thermoelectric effects in graphene nanostructures. Journal of Physics: Condensed Matter, 27(13), 133204.

[2] Markov, M., & Zebarjadi, M. (2019). Thermoelectric transport in graphene and 2D layered materials. Nanoscale and Microscale Thermophysical Engineering, 23(2), 117-127.

[3] M. Zebarjadi, Electronic cooling using thermoelectric devices, Appl. Phys. Lett. 106 (2015) 203506. https://doi.org/10.1063/1.4921457.

[4] M.J. Adams, M. Verosky, M. Zebarjadi, J.P. Heremans, Active Peltier Coolers Based on Correlated and Magnon-Drag Metals, Phys. Rev. Appl. 11 (2019) 054008. https://doi.org/10.1103/PhysRevApplied.11.054008.

[5] J. Duan, X. Wang, X. Lai, G. Li, K. Watanabe, T. Taniguchi, M. Zebarjadi, E.Y. Andrei, High thermoelectricpower factor in graphene/hBN devices, Proc. Natl. Acad. Sci. 113 (2016) 14272–14276. https://doi.org/10.1073/pnas.1615913113.

[6] Lundstrom, M. S., & Jeong, C. (2012). Near-Equilibrium Transport: Fundamentals and Applications (Vol. 2). World Scientific Publishing Company.

[7] Jeong, C., Kim, R., Luisier, M., Datta, S., & Lundstrom, M. (2010). On Landauer versus Boltzmann and full band versus effective mass evaluation of thermoelectric transport coefficients. Journal of Applied Physics, 107(2), 023707.

[8] Fisher, Timothy S. Thermal energy at the nanoscale. Vol. 3. World Scientific Publishing Company, 2013.

[9] Mahan, G. D.; Sofo, J. O. The best thermoelectric. Proceedings of the National Academy of Sciences, 1996, 93.15: 7436-7439.

[10] Seol, J. H., Jo, I., Moore, A. L., Lindsay, L., Aitken, Z. H., Pettes, M. T., ... & Mingo, N. (2010). Two-dimensional phonon transport in supported graphene. Science, 328(5975), 213-216.

[11] Y.M. Zuev, W. Chang, P. Kim, Thermoelectric and Magnetothermoelectric Transport Measurements of Graphene, Phys. Rev. Lett. 102 (2009) 096807. https://doi.org/10.1103/PhysRevLett.102.096807.

[12] Hippalgaonkar, K., Wang, Y., Ye, Y., Qiu, D. Y., Zhu, H., Wang, Y., ... & Zhang, X. (2017). High thermoelectric power factor in two-dimensional crystals of MoS_2. Physical Review B, 95(11), 115407.

[13] Hicks, L. D., and Dresselhaus, M. S. "Effect of quantum-well structures on the thermoelectric figure of merit." Physical Review B 47.19 (1993): 12727.

[14] Hicks, L. D., and Dresselhaus, M. S. "Thermoelectric figure of merit of a one-dimensional conductor." Physical review B 47.24 (1993): 16631.

941 [15] Mao, J., Liu, Z., & Ren, Z. (2016). Size effect in thermoelectric materials. npj Quantum
942 Materials, 1(1), 1-9.

943 [16] Xiao, Y., Chen, Q., Ma, D., Yang, N., & Hao, Q. (2019). Phonon Transport within Periodic
944 Porous Structures--From Classical Phonon Size Effects to Wave Effects. ES Materials &
945 Manufacturing, 5, 2-18.

946 [17] Novoselov, K. S., Mishchenko, A., Carvalho, A., & Neto, A. C. (2016). 2D materials and
947 van der Waals heterostructures. Science, 353(6298), aac9439.

948 [18] Geim, A. K., & Grigorieva, I. V. (2013). Van der Waals heterostructures. Nature,
949 499(7459), 419-425.

950 [19] Mounet, N., Gibertini, M., Schwaller, P., Campi, D., Merkys, A., Marrazzo, A., ... &
951 Marzari, N. (2018). Two-dimensional materials from high-throughput computational
952 exfoliation of experimentally known compounds. Nature nanotechnology, 13(3), 246-252.

953 [20] Xu, Y., Li, Z., & Duan, W. (2014). Thermal and thermoelectric properties of
954 graphene. Small, 10(11), 2182-2199.

955 [21] Zhang, G., & Zhang, Y. W. (2017). Thermoelectric properties of two-dimensional
956 transition metal dichalcogenides. Journal of Materials Chemistry C, 5(31), 7684-7698.

957 [22] Jing Wu, Yabin Chen, Junqiao Wu, Kedar Hippalgaonkar. Perspectives on
958 Thermoelectricity in Layered and 2D Materials. Advanced Electronic Materials 2018, 4
959 (12) , 1800248. DOI: 10.1002/aelm.201800248.

960 [23] Zhao, Y., Cai, Y., Zhang, L., Li, B., Zhang, G., & Thong, J. T. (2019). Thermal Transport
961 in 2D Semiconductors—Considerations for Device Applications. Advanced Functional
962 Materials, 1903929.

963 [24] Kanahashi, Kaito; Pu, Jiang; Takenobu, Taishi. 2D Materials for Large-Area Flexible
964 Thermoelectric Devices. Advanced Energy Materials, 2019, 1902842.

965 [25] Zong, P. A., Liang, J., Zhang, P., Wan, C., Wang, Y., & Koumoto, K. (2020). Graphene-
966 Based Thermoelectrics. ACS Applied Energy Materials, 3(3), 2224-2239.

967 [26] Li, D., Gong, Y., Chen, Y., Lin, J., Khan, Q., Zhang, Y., ... & Xie, H. (2020). Recent
968 Progress of Two-Dimensional Thermoelectric Materials. Nano-Micro Letters, 12(1), 36.

969 [27] Sankeshwar, N. S., Kubakaddi, S. S., & Mulimani, B. G. (2013). Thermoelectric power in
970 graphene. Advances in Graphene Science, 10, 56720.

971 [28] Wei P, Bao W, Pu Y, Lau C and Shi J 2009 Anomalous thermoelectric transport of dirac
972 particles in graphene Phys. Rev. Lett. 102 166808

973 [29] Checkelsky J and Ong N 2009 Thermopower and Nernst effect in graphene in a magnetic
974 field Phys. Rev. B 80 081413

975 [30] Wu X, Hu Y, Ruan M, Madiomanana N K, Berger C and de Heer W A 2011
976 Thermoelectric effect in high mobility single layer epitaxial graphene Appl. Phys. Lett. 99
977 133102

978 [31] Sadeghi, M. M., Jo, I., & Shi, L. (2013). Phonon-interface scattering in multilayer
979 graphene on an amorphous support. Proceedings of the National Academy of
980 Sciences, 110(41), 16321-16326.

981 [32] Pop, E., Varshney, V., & Roy, A. K. (2012). Thermal properties of graphene:
982 Fundamentals and applications. MRS bulletin, 37(12), 1273-1281.

983 [33] Balandin, A. A. (2011). Thermal properties of graphene and nanostructured carbon
984 materials. Nature materials, 10(8), 569-581.

985 [34] Li, Q. Y., Xia, K., Zhang, J., Zhang, Y., Li, Q., Takahashi, K., & Zhang, X. (2017).
986 Measurement of specific heat and thermal conductivity of supported and suspended
987 graphene by a comprehensive Raman optothermal method. Nanoscale, 9(30), 10784-
988 10793.

989 [35] Gu, X., Fan, Z., Bao, H., & Zhao, C. Y. (2019). Revisiting phonon-phonon scattering in
990 single-layer graphene. Physical Review B, 100(6), 064306.

991 [36] Zhang, Y., Tang, T. T., Girit, C., Hao, Z., Martin, M. C., Zettl, A., ... & Wang, F. (2009).
992 Direct observation of a widely tunable bandgap in bilayer graphene. Nature, 459(7248),
993 820-823.

994 [37] Lui, C. H., Li, Z., Mak, K. F., Cappelluti, E., & Heinz, T. F. (2011). Observation of an
995 electrically tunable band gap in trilayer graphene. Nature Physics, 7(12), 944-947.

996 [38] Bao, W., Jing, L., Velasco, J., Lee, Y., Liu, G., Tran, D., ... & Koshino, M. (2011).
997 Stacking-dependent band gap and quantum transport in trilayer graphene. Nature
998 Physics, 7(12), 948-952.

999 [39] Cao, Y., Fatemi, V., Fang, S., Watanabe, K., Taniguchi, T., Kaxiras, E., & Jarillo-Herrero,
1000 P. (2018). Unconventional superconductivity in magic-angle graphene
1001 superlattices. Nature, 556(7699), 43-50.

1002 [40] Nam S-G, Ki D-K and Lee H-J 2010 Thermoelectric transport of massive Dirac fermions
1003 in bilayer graphene Phys. Rev. B 82 245416

1004 [41] Wang, C. R., Lu, W. S., Hao, L., Lee, W. L., Lee, T. K., Lin, F., ... & Chen, J. Z. (2011).
1005 Enhanced thermoelectric power in dual-gated bilayer graphene. Physical review
1006 letters, 107(18), 186602.

1007 [42] Chien, Y. Y., Yuan, H., Wang, C. R., & Lee, W. L. (2016). Thermoelectric power in
1008 bilayer graphene device with ionic liquid gating. Scientific reports, 6, 20402.

1009 [43] Suszalski, D., Rut, G., & Rycerz, A. (2019). Thermoelectric properties of gapped bilayer
1010 graphene. Journal of Physics: Condensed Matter, 31(41), 415501.

[44] Manzeli, S., Ovchinnikov, D., Pasquier, D., Yazyev, O. V., & Kis, A. (2017). 2D transition metal dichalcogenides. Nature Reviews Materials, 2(8), 17033.

[45] Huang, W., Da, H., & Liang, G. (2013). Thermoelectric performance of MX_2 (M= Mo, W; X= S, Se) monolayers. Journal of Applied Physics, 113(10), 104304.

[46] Wickramaratne, D., Zahid, F., & Lake, R. K. (2014). Electronic and thermoelectric properties of few-layer transition metal dichalcogenides. The Journal of chemical physics, 140(12), 124710.

[47] Huang, W., Luo, X., Gan, C. K., Quek, S. Y., & Liang, G. (2014). Theoretical study of thermoelectric properties of few-layer MoS_2 and WSe_2. Physical Chemistry Chemical Physics, 16(22), 10866-10874.

[48] Wu, J., Schmidt, H., Amara, K. K., Xu, X., Eda, G., & Özyilmaz, B. (2014). Large thermoelectricity via variable range hopping in chemical vapor deposition grown single-layer MoS_2. Nano Letters, 14(5), 2730-2734.

[49] M. Kayyalha, J. Maassen, M. Lundstrom, L. Shi, Y.P. Chen, Gate-tunable and thickness-dependent electronic and thermoelectric transport in few-layer MoS2, J. Appl. Phys. 120 (2016) 134305. https://doi.org/10.1063/1.4963364.

[50] Jin, Z., Liao, Q., Fang, H., Liu, Z., Liu, W., Ding, Z., ... & Yang, N. (2015). A revisit to high thermoelectric performance of single-layer MoS_2. Scientific reports, 5, 18342.

[51] Li, Z., Lv, Y., Ren, L., Li, J., Kong, L., Zeng, Y., ... & Wang, D. (2020). Efficient strain modulation of 2D materials via polymer encapsulation. Nature communications, 11(1), 1-8.

[52] Yoshida, M., Iizuka, T., Saito, Y., Onga, M., Suzuki, R., Zhang, Y., ... & Shimizu, S. (2016). Gate-optimized thermoelectric power factor in ultrathin WSe_2 single crystals. Nano Letters, 16(3), 2061-2065.

[53] Liu, J., Choi, G. M., & Cahill, D. G. (2014). Measurement of the anisotropic thermal conductivity of molybdenum disulfide by the time-resolved magneto-optic Kerr effect. Journal of Applied Physics, 116(23), 233107.

[54] Jiang, P., Qian, X., Gu, X., & Yang, R. (2017). Probing Anisotropic Thermal Conductivity of Transition Metal Dichalcogenides MX_2 (M= Mo, W and X= S, Se) using Time‐Domain Thermoreflectance. Advanced Materials, 29(36), 1701068.

[55] Chiritescu, C., Cahill, D. G., Nguyen, N., Johnson, D., Bodapati, A., Keblinski, P., & Zschack, P. (2007). Ultralow thermal conductivity in disordered, layered WSe_2 crystals. Science, 315(5810), 351-353.

[56] Lindroth, D. O., & Erhart, P. (2016). Thermal transport in van der Waals solids from first-principles calculations. Physical Review B, 94(11), 115205.

[57] Yan, R., Simpson, J. R., Bertolazzi, S., Brivio, J., Watson, M., Wu, X., ... & Xing, H. G. (2014). Thermal conductivity of monolayer molybdenum disulfide obtained from temperature-dependent Raman spectroscopy. ACS Nano, 8(1), 986-993.

[58] Yu, Y., Minhaj, T., Huang, L., Yu, Y., & Cao, L. (2020). In-Plane and Interfacial Thermal Conduction of Two-Dimensional Transition-Metal Dichalcogenides. Physical Review Applied, 13(3), 034059.

[59] Yuan, P., Wang, R., Wang, T., Wang, X., & Xie, Y. (2018). Nonmonotonic thickness-dependence of in-plane thermal conductivity of few-layered MoS_2: 2.4 to 37.8 nm. Physical Chemistry Chemical Physics, 20(40), 25752-25761.

[60] Yuan, P., Wang, R., Tan, H., Wang, T., & Wang, X. (2017). Energy Transport State Resolved Raman for Probing Interface Energy Transport and Hot Carrier Diffusion in Few-Layered MoS_2. ACS Photonics, 4(12), 3115-3129.

[61] Wang, R., Wang, T., Zobeiri, H., Yuan, P., Deng, C., Yue, Y., ... & Wang, X. (2018). Measurement of the thermal conductivities of suspended MoS_2 and $MoSe_2$ by nanosecond ET-Raman without temperature calibration and laser absorption evaluation. Nanoscale, 10(48), 23087-23102.

[62] Wang, R., Zobeiri, H., Xie, Y., Wang, X., Zhang, X., & Yue, Y. (2020) Distinguishing Optical and Acoustic Phonon Temperatures and Their Energy Coupling Factor under Photon Excitation in nm 2D Materials. Advanced Science, 2000097.

[63] N. Peimyoo, J. Shang, W. Yang, Y. Wang, C. Cong, and T. Yu, Thermal conductivity determination of suspended mono-and bilayer WS_2 by Raman spectroscopy, Nano Res. 8, 1210 (2015).

[64] Jo, I., Pettes, M. T., Ou, E., Wu, W., & Shi, L. (2014). Basal-plane thermal conductivity of few-layer molybdenum disulfide. Applied Physics Letters, 104(20), 201902.

[65] Yarali, M., Wu, X., Gupta, T., Ghoshal, D., Xie, L., Zhu, Z., ... & Koratkar, N. (2017). Effects of Defects on the Temperature‐Dependent Thermal Conductivity of Suspended Monolayer Molybdenum Disulfide Grown by Chemical Vapor Deposition. Advanced Functional Materials, 27(46), 1704357.

[66] Aiyiti, A., Bai, X., Wu, J., Xu, X., & Li, B. (2018). Measuring the thermal conductivity and interfacial thermal resistance of suspended MoS_2 using electron beam self-heating technique. Science Bulletin, 63(7), 452-458.

[67] Gu, X., & Yang, R. (2014). Phonon transport in single-layer transition metal dichalcogenides: A first-principles study. Applied Physics Letters, 105(13), 131903.

[68] Xu, K., Gabourie, A. J., Hashemi, A., Fan, Z., Wei, N., Farimani, A. B., ... & Ala-Nissila, T. (2019). Thermal transport in MoS_2 from molecular dynamics using different empirical potentials. Physical Review B, 99(5), 054303.

[69] Gu, X., Li, B., & Yang, R. (2016). Layer thickness-dependent phonon properties and thermal conductivity of MoS_2. Journal of Applied Physics, 119(8), 085106.

[70] Zhou, W. X., & Chen, K. Q. (2015). First-principles determination of ultralow thermal conductivity of monolayer WSe_2. Scientific reports, 5, 15070.

[71] Wan, C., Gu, X., Dang, F., Itoh, T., Wang, Y., Sasaki, H., ... & Yang, R. (2015). Flexible n-type thermoelectric materials by organic intercalation of layered transition metal dichalcogenide TiS_2. Nature Materials, 14(6), 622-627.

[72] Li, L., Yu, Y., Ye, G. J., Ge, Q., Ou, X., Wu, H., ... & Zhang, Y. (2014). Black phosphorus field-effect transistors. Nature nanotechnology, 9(5), 372.

[73] Luo, Z., Maassen, J., Deng, Y., Du, Y., Garrelts, R. P., Lundstrom, M. S., ... & Xu, X. (2015). Anisotropic in-plane thermal conductivity observed in few-layer black phosphorus. Nature communications, 6(1), 1-8.

[74] Jang, H., Wood, J. D., Ryder, C. R., Hersam, M. C., & Cahill, D. G. (2015). Anisotropic thermal conductivity of exfoliated black phosphorus. Advanced Materials, 27(48), 8017-8022.

[75] Lee, S., Yang, F., Suh, J., Yang, S., Lee, Y., Li, G., ... & Park, J. (2015). Anisotropic in-plane thermal conductivity of black phosphorus nanoribbons at temperatures higher than 100 K. Nature communications, 6(1), 1-7.

[76] Smith, B., Vermeersch, B., Carrete, J., Ou, E., Kim, J., Mingo, N., ... & Shi, L. (2017). Temperature and thickness dependences of the anisotropic in-plane thermal conductivity of black phosphorus. Advanced Materials, 29(5), 1603756.

[77] Lv, H.Y., Lu, W.J., Shao, D.F. and Sun, Y.P., 2014. Enhanced thermoelectric performance of phosphorene by strain-induced band convergence. Physical Review B, 90(8), p.085433.

[78] Qin, G., Yan, Q. B., Qin, Z., Yue, S. Y., Cui, H. J., Zheng, Q. R., & Su, G. (2014). Hinge-like structure induced unusual properties of black phosphorus and new strategies to improve the thermoelectric performance. Scientific reports, 4, 6946.

[79] Flores, E., Ares, J. R., Castellanos-Gomez, A., Barawi, M., Ferrer, I. J., & Sánchez, C. (2015). Thermoelectric power of bulk black-phosphorus. Applied Physics Letters, 106(2), 022102.

[80] Saito, Y., Iizuka, T., Koretsune, T., Arita, R., Shimizu, S., & Iwasa, Y. (2016). Gate-tuned thermoelectric power in black phosphorus. Nano letters, 16(8), 4819-4824.

[81] Fei, R., Faghaninia, A., Soklaski, R., Yan, J. A., Lo, C., & Yang, L. (2014). Enhanced thermoelectric efficiency via orthogonal electrical and thermal conductances in phosphorene. Nano letters, 14(11), 6393-6399.

[82] Choi, S. J., Kim, B. K., Lee, T. H., Kim, Y. H., Li, Z., Pop, E., ... & Bae, M. H. (2016). Electrical and thermoelectric transport by variable range hopping in thin black phosphorus devices. Nano letters, 16(7), 3969-3975.

[83] Zare, M., Rameshti, B. Z., Ghamsari, F. G., & Asgari, R. (2017). Thermoelectric transport in monolayer phosphorene. Physical Review B, 95(4), 045422.

[84] Zhao, L. D., Lo, S. H., Zhang, Y., Sun, H., Tan, G., Uher, C., ... & Kanatzidis, M. G. (2014). Ultralow thermal conductivity and high thermoelectric figure of merit in SnSe crystals. Nature, 508(7496), 373-377.

[85] Heo, S. H., Jo, S., Kim, H. S., Choi, G., Song, J. Y., Kang, J. Y., ... & Jung, J. (2019). Composition change-driven texturing and doping in solution-processed SnSe thermoelectric thin films. Nature communications, 10(1), 1-10.

[86] Shi, X. L., Tao, X., Zou, J., & Chen, Z. G. (2020). High‐Performance Thermoelectric SnSe: Aqueous Synthesis, Innovations, and Challenges. Advanced Science, 7(7), 1902923.

[87] Zhao, L. D., Chang, C., Tan, G., & Kanatzidis, M. G. (2016). SnSe: a remarkable new thermoelectric material. Energy & Environmental Science, 9(10), 3044-3060.

[88] Zhou, Y., & Zhao, L. D. (2017). Promising thermoelectric bulk materials with 2D structures. Advanced Materials, 29(45), 1702676.

[89] Lin, S., Li, W., Chen, Z., Shen, J., Ge, B., & Pei, Y. (2016). Tellurium as a high-performance elemental thermoelectric. Nature communications, 7(1), 1-6.

[90] Sharma, S., Singh, N., & Schwingenschlögl, U. (2018). Two-dimensional tellurene as excellent thermoelectric material. ACS Applied Energy Materials, 1(5), 1950-1954.

[91] Gao, Z., Liu, G., & Ren, J. (2018). High thermoelectric performance in two-dimensional tellurium: An ab initio study. ACS applied materials & interfaces, 10(47), 40702-40709.

[92] Qiu, G., Huang, S., Segovia, M., Venuthurumilli, P. K., Wang, Y., Wu, W., ... & Ye, P. D. (2019). Thermoelectric performance of 2D tellurium with accumulation contacts. Nano letters, 19(3), 1955-1962.

[93] Zhang, X., Liu, C., Tao, Y., Li, Y., Guo, Y., Chen, Y., ... & Wang, J. (2020). High ZT 2D Thermoelectrics by Design: Strong Interlayer Vibration and Complete Band‐Extrema Alignment. Advanced Functional Materials.

[94] S. Shimizu, J. Shiogai, N. Takemori, S. Sakai, H. Ikeda, R. Arita, T. Nojima, A. Tsukazaki, Y. Iwasa, Giant thermoelectric power factor in ultrathin FeSe superconductor, Nat. Commun. 10 (2019). https://doi.org/10.1038/s41467-019-08784-z.

[95] Lee, M. J., Ahn, J. H., Sung, J. H., Heo, H., Jeon, S. G., Lee, W., ... & Jo, M. H. (2016). Thermoelectric materials by using two-dimensional materials with negative correlation between electrical and thermal conductivity. Nature Communications, 7(1), 1-7.

[96] Shimizu, S., Bahramy, M. S., Iizuka, T., Ono, S., Miwa, K., Tokura, Y., & Iwasa, Y. (2016). Enhanced thermopower in ZnO two-dimensional electron gas. Proceedings of the National Academy of Sciences, 113(23), 6438-6443.

[97] Hung, N. T., Nugraha, A. R., & Saito, R. (2017). Two-dimensional InSe as a potential thermoelectric material. Applied Physics Letters, 111(9), 092107.

[98] Sharma, S., Kumar, S., & Schwingenschlögl, U. (2017). Arsenene and antimonene: two-dimensional materials with high thermoelectric figures of merit. Physical Review Applied, 8(4), 044013.

[99] Yu, J., Li, T., & Sun, Q. (2019). Single-layer BiOBr: An effective p-type 2D thermoelectric material. Journal of Applied Physics, 125(20), 205111.

[100] Esfarjani, K., Chen, G., & Stokes, H. T. (2011). Heat transport in silicon from first-principles calculations. Physical Review B, 84(8), 085204.

[101] Zhang, W., Fisher, T. & Mingo, N. The atomistic Green's function method: An efficient simulation approach for nanoscale phonon transport. Numerical Heat Transfer, Part B: Fundamentals 51, 333-349 (2007).

[102] S. Datta, Electronic Transport in Mesoscopic Systems (Cambridge University Press, 1997).

[103] Cepellotti, A., Fugallo, G., Paulatto, L., Lazzeri, M., Mauri, F., & Marzari, N. (2015). Phonon hydrodynamics in two-dimensional materials. Nature communications, 6(1), 1-7.

[104] Lee, S., Broido, D., Esfarjani, K., & Chen, G. (2015). Hydrodynamic phonon transport in suspended graphene. Nature communications, 6(1), 1-10.

[105] Lee, S., & Li, X. (2019). (invited book chapter) Hydrodynamic Phonon Transport: Past, Present, and Prospect. In Nanoscale Energy Transport: Emerging Phenomena, Methods, and Applications, Liao, B. (Ed.). Institute of Physics Publishing

[106] Li, X., & Lee, S. (2019). Crossover of ballistic, hydrodynamic, and diffusive phonon transport in suspended graphene. PHYSICAL REVIEW B, 99(8).

[107] Mezhov-Deglin, L. Measurement of the thermal conductivity of crystalline He4. J. Exp. Theor. Phys. 49, 66–79 (1965).

[108] Huberman, S., Duncan, R. A., Chen, K., Song, B., Chiloyan, V., Ding, Z., ... & Nelson, K. A. (2019). Observation of second sound in graphite at temperatures above 100 K. Science, 364(6438), 375-379.

[109] Shang, M. Y., Zhang, C., Guo, Z., & Lü, J. T. (2020). Heat vortex in hydrodynamic phonon transport of two-dimensional materials. Scientific Reports, 10(1), 1-10.

[110] Wang, X. M., Mo, D. C., & Lu, S. S. (2013). On the thermoelectric transport properties of graphyne by the first-principles method. The Journal of chemical physics, 138(20), 204704.

[111] Gu, X., & Yang, R. (2016). Phonon transport and thermal conductivity in two-dimensional materials. Annual Review of Heat Transfer, 19.

[112] W.J. Evans, L. Hu, and P. Keblinski, Thermal conductivity of graphene ribbons from equilibrium molecular dynamics: Effect of ribbon width, edge roughness, and hydrogen termination, Appl. Phys. Lett., Vol. 96, p. 203112, 2010.

[113] Feng, T., Ruan, X., Ye, Z., & Cao, B. (2015). Spectral phonon mean free path and thermal conductivity accumulation in defected graphene: The effects of defect type and concentration. Physical Review B, 91(22), 224301.

[114] Girit, Ç. Ö., Meyer, J. C., Erni, R., Rossell, M. D., Kisielowski, C., Yang, L., Park, C.-H., Crommie, M., Cohen, M. L. & Louie, S. G. Graphene at the edge: stability and dynamics. Science 323, 1705-1708 (2009).

[115] Z. Guo, D. Zhang, and X.-G. Gong, Thermal conductivity of graphene nanoribbons, Appl. Phys. Lett., Vol. 95, p. 163103, 2009.

[116] Munoz, E., Lu, J., & Yakobson, B. I. (2010). Ballistic thermal conductance of graphene ribbons. Nano letters, 10(5), 1652-1656.

[117] Z. Wei, Y. Chen, and C. Dames, Wave packet simulations of phonon boundary scattering at graphene edges, J. Appl. Phys., Vol. 112, p. 024328, 2012.

[118] Ouyang, Y., & Guo, J. (2009). A theoretical study on thermoelectric properties of graphene nanoribbons. Applied Physics Letters, 94(26), 263107.

[119] Sevinçli, H., & Cuniberti, G. (2010). Enhanced thermoelectric figure of merit in edge-disordered zigzag graphene nanoribbons. Physical Review B, 81(11), 113401.

[120] Haskins, J., Kınacı, A., Sevik, C., Sevinçli, H., Cuniberti, G., & Çağın, T. (2011). Control of thermal and electronic transport in defect-engineered graphene nanoribbons. ACS nano, 5(5), 3779-3787.

[121] Karamitaheri, H., Neophytou, N., Pourfath, M., Faez, R., & Kosina, H. (2012). Engineering enhanced thermoelectric properties in zigzag graphene nanoribbons. Journal of Applied Physics, 111(5), 054501.

[122] Zheng, H., Liu, H. J., Tan, X. J., Lv, H. Y., Pan, L., Shi, J., & Tang, X. F. (2012). Enhanced thermoelectric performance of graphene nanoribbons. Applied Physics Letters, 100(9), 093104.

[123] Tran, V. T., Saint-Martin, J., Dollfus, P., & Volz, S. (2017). Optimizing the thermoelectric performance of graphene nanoribbons without degrading the electronic properties. Scientific reports, 7(1), 1-11.

[124] Shihua Tan, Ke-Qiu Chen. The enhancement of the thermoelectric performance in zigzag graphene nanoribbon by edge states. Carbon 2015, 94, 942-945. DOI: 10.1016/j.carbon.2015.07.083.

[125] Sevinçli, H., Sevik, C., Çağın, T., & Cuniberti, G. (2013). A bottom-up route to enhance thermoelectric figures of merit in graphene nanoribbons. Scientific reports, 3(1), 1-6.

[126] Pan, C. N., Xie, Z. X., Tang, L. M., & Chen, K. Q. (2012). Ballistic thermoelectric properties in graphene-nanoribbon-based heterojunctions. Applied Physics Letters, 101(10), 103115.

[127] Mazzamuto, F., Nguyen, V. H., Apertet, Y., Caër, C., Chassat, C., Saint-Martin, J., & Dollfus, P. (2011). Enhanced thermoelectric properties in graphene nanoribbons by resonant tunneling of electrons. Physical Review B, 83(23), 235426.

[128] Yeo, P. S. E., Sullivan, M. B., Loh, K. P., & Gan, C. K. (2013). First-principles study of the thermoelectric properties of strained graphene nanoribbons. Journal of Materials Chemistry A, 1(36), 10762-10767.

[129] Wei, N., Xu, L., Wang, H. Q., & Zheng, J. C. (2011). Strain engineering of thermal conductivity in graphene sheets and nanoribbons: a demonstration of magic flexibility. Nanotechnology, 22(10), 105705.

[130] Liang, L., Cruz-Silva, E., Girão, E. C., & Meunier, V. (2012). Enhanced thermoelectric figure of merit in assembled graphene nanoribbons. Physical Review B, 86(11), 115438.

[131] Mazzamuto, F., Saint-Martin, J., Nguyen, V. H., Chassat, C., & Dollfus, P. (2012). Thermoelectric performance of disordered and nanostructured graphene ribbons using Green's function method. Journal of Computational Electronics, 11(1), 67-77.

[132] Yan, Y., Liang, Q. F., Zhao, H., & Wu, C. Q. (2012). Thermoelectric properties of hexagonal graphene quantum dots. Physics Letters A, 376(12-13), 1154-1158.

[133] Ni, X., Liang, G., Wang, J. S., & Li, B. (2009). Disorder enhances thermoelectric figure of merit in armchair graphane nanoribbons. Applied Physics Letters, 95(19), 192114.

[134] Yang, K., Cahangirov, S., Cantarero, A., Rubio, A., & D'Agosta, R. (2014). Thermoelectric properties of atomically thin silicene and germanene nanostructures. Physical Review B, 89(12), 125403.

[135] Zberecki, K., Wierzbicki, M., Barnaś, J., & Swirkowicz, R. (2013). Thermoelectric effects in silicene nanoribbons. Physical Review B, 88(11), 115404.

[136] Zberecki, K., Swirkowicz, R., & Barnaś, J. (2014). Spin effects in thermoelectric properties of Al-and P-doped zigzag silicene nanoribbons. Physical Review B, 89(16), 165419.

[137] Fan, D. D., Liu, H. J., Cheng, L., Jiang, P. H., Shi, J., & Tang, X. F. (2014). MoS2 nanoribbons as promising thermoelectric materials. Applied Physics Letters, 105(13), 133113.

[138] Chen, K. X., Luo, Z. Y., Mo, D. C., & Lyu, S. S. (2016). WSe2 nanoribbons: new high-performance thermoelectric materials. Physical Chemistry Chemical Physics, 18(24), 16337-16344.

[139] Wang, J., Xie, F., Cao, X. H., An, S. C., Zhou, W. X., Tang, L. M., & Chen, K. Q. (2017). Excellent Thermoelectric Properties in monolayer WSe2 Nanoribbons due to Ultralow Phonon Thermal Conductivity. Scientific reports, 7(1), 1-8.

[140] Zhang, J., Liu, H. J., Cheng, L., Wei, J., Liang, J. H., Fan, D. D., ... & Zhang, Q. J. (2014). Phosphorene nanoribbon as a promising candidate for thermoelectric applications. Scientific reports, 4(1), 1-8.

[141] Chen, X. K., Xie, Z. X., Zhou, W. X., Tang, L. M., & Chen, K. Q. (2016). Phonon wave interference in graphene and boron nitride superlattice. Applied Physics Letters, 109(2), 023101.

[142] Felix, I. M., & Pereira, L. F. C. (2018). Thermal conductivity of graphene-hBN superlattice ribbons. Scientific reports, 8(1), 2737.

[143] Tran, V. T., Saint-Martin, J., & Dollfus, P. (2015). High thermoelectric performance in graphene nanoribbons by graphene/BN interface engineering. Nanotechnology, 26(49), 495202.

[144] Yokomizo, Y., & Nakamura, J. (2013). Giant Seebeck coefficient of the graphene/h-BN superlattices. Applied Physics Letters, 103(11), 113901.

[145] Yang, K., Chen, Y., D'Agosta, R., Xie, Y., Zhong, J., & Rubio, A. (2012). Enhanced thermoelectric properties in hybrid graphene/boron nitride nanoribbons. Physical Review B, 86(4), 045425.

[146] Zhang, Z., Xie, Y., Peng, Q., & Chen, Y. (2016). A theoretical prediction of super high-performance thermoelectric materials based on MoS_2/WS_2 hybrid nanoribbons. Scientific reports, 6, 21639.

[147] Ouyang, Y., Xie, Y., Zhang, Z., Peng, Q., & Chen, Y. (2016). Very high thermoelectric figure of merit found in hybrid transition-metal-dichalcogenides. Journal of Applied Physics, 120(23), 235109.

[148] Oswald W and Wu Z 2012 Energy gaps in graphene nanomeshes Phys. Rev. B 85 115431

[149] Ouyang, F., Peng, S., Liu, Z., & Liu, Z. (2011). Bandgap opening in graphene antidot lattices: the missing half. ACS nano, 5(5), 4023-4030.

[150] Vanević, M., Stojanović, V. M., & Kindermann, M. (2009). Character of electronic states in graphene antidot lattices: Flat bands and spatial localization. Physical Review B, 80(4), 045410.

[151] Pedersen, T. G., Flindt, C., Pedersen, J., Mortensen, N. A., Jauho, A. P., & Pedersen, K. (2008). Graphene antidot lattices: designed defects and spin qubits. Physical Review Letters, 100(13), 136804.

[152] Yang, L., Chen, J., Yang, N., & Li, B. (2015). Significant reduction of graphene thermal conductivity by phononic crystal structure. International Journal of Heat and Mass Transfer, 91, 428-432.

[153] Tianli Feng, Xiulin Ruan. Ultra-low thermal conductivity in graphene nanomesh. Carbon 2016, 101, 107-113.

[154] Gunst, T., Markussen, T., Jauho, A. P., & Brandbyge, M. (2011). Thermoelectric properties of finite graphene antidot lattices. Physical Review B, 84(15), 155449.

[155] Karamitaheri, H., Pourfath, M., Faez, R., & Kosina, H. (2011). Geometrical effects on the thermoelectric properties of ballistic graphene antidot lattices. Journal of Applied Physics, 110(5), 054506.

[156] Yan, Y., Liang, Q. F., Zhao, H., Wu, C. Q., & Li, B. (2012). Thermoelectric properties of one-dimensional graphene antidot arrays. Physics Letters A, 376(35), 2425-2429.

[157] Hossain, M. S., Al-Dirini, F., Hossain, F. M., & Skafidas, E. (2015). High performance graphene nano-ribbon thermoelectric devices by incorporation and dimensional tuning of nanopores. Scientific reports, 5, 11297.

[158] Chang, P. H., Bahramy, M. S., Nagaosa, N., & Nikolic, B. K. (2014). Giant thermoelectric effect in graphene-based topological insulators with heavy adatoms and nanopores. Nano letters, 14(7), 3779-3784.

[159] Sadeghi, H., Sangtarash, S., & Lambert, C. J. (2015). Enhanced thermoelectric efficiency of porous silicene nanoribbons. Scientific reports, 5, 9514.

[160] Shao, L., Chen, G., Ye, H., Wu, Y., Niu, H., & Zhu, Y. (2014). Theoretical study on electronic properties of MoS2 antidot lattices. Journal of Applied Physics, 116(11), 113704.

[161] Cupo, A., Masih Das, P., Chien, C. C., Danda, G., Kharche, N., Tristant, D., ... & Meunier, V. (2017). Periodic arrays of phosphorene nanopores as antidot lattices with tunable properties. ACS Nano, 11(7), 7494-7507.

[162] Yamawaki, M., Ohnishi, M., Ju, S., & Shiomi, J. (2018). Multifunctional structural design of graphene thermoelectrics by Bayesian optimization. Science Advances, 4(6), eaar4192.

[163] Wei, H., Bao, H., & Ruan, X. (2020). Genetic algorithm-driven discovery of unexpected thermal conductivity enhancement by disorder. Nano Energy, 71, 104619.

[164] Ju, S., Shiga, T., Feng, L., Hou, Z., Tsuda, K., & Shiomi, J. (2017). Designing nanostructures for phonon transport via Bayesian optimization. Physical Review X, 7(2), 021024.

[165] Wan, X., Feng, W., Wang, Y., Wang, H., Zhang, X., Deng, C., & Yang, N. (2019). Materials Discovery and Properties Prediction in Thermal Transport via Materials Informatics: A Mini Review. Nano letters, 19(6), 3387-3395.

[166] Wang, T., Zhang, C., Snoussi, H., & Zhang, G. (2020). Machine Learning Approaches for Thermoelectric Materials Research. Advanced Functional Materials, 30(5), 1906041.

[167] Wu, D., Yu, Z., Xiao, J., & Ouyang, F. (2010). The chemical modification of graphene antidot lattices. Physica E: Low-dimensional Systems and Nanostructures, 43(1), 33-39.

[168] Liu, X., Zhang, Z., & Guo, W. (2013). Universal rule on chirality‐dependent bandgaps in graphene antidot lattices. Small, 9(8), 1405-1410.

[169] Ji, X., Zhang, J., Wang, Y., Qian, H., & Yu, Z. (2013). Influence of edge imperfections on the transport behavior of graphene nanomeshes. Nanoscale, 5(6), 2527-2531.

[170] Dvorak, M., Oswald, W., & Wu, Z. (2013). Bandgap opening by patterning graphene. Scientific reports, 3(1), 1−7.

[171] Brun, S. J., Thomsen, M. R., & Pedersen, T. G. (2014). Electronic and optical properties of graphene antidot lattices: comparison of Dirac and tight-binding models. Journal of Physics: Condensed Matter, 26(26), 265301.

[172] Yuan, S., Roldán, R., Jauho, A. P., & Katsnelson, M. I. (2013). Electronic properties of disordered graphene antidot lattices. Physical Review B, 87(8), 085430.

[173] Fürst, J. A., Pedersen, J. G., Flindt, C., Mortensen, N. A., Brandbyge, M., Pedersen, T. G., & Jauho, A. P. (2009). Electronic properties of graphene antidot lattices. New Journal of Physics, 11(9), 095020.

[174] Hung Nguyen, V., Chung Nguyen, M., Nguyen, H.-V. & Dollfus, P. Disorder effects on electronic bandgap and transport in graphene-nanomesh-based structures. Journal of Applied Physics 113, 013702 (2013).

[175] Kim, M., Safron, N. S., Han, E., Arnold, M. S. & Gopalan, P. Fabrication and characterization of large-area, semiconducting nanoperforated graphene materials. Nano letters 10, 1125-1131 (2010).

[176] Bai, J., Zhong, X., Jiang, S., Huang, Y. & Duan, X. Graphene nanomesh. Nature nanotechnology 5, 190-194 (2010).

[177] Shi, L., Li, D., Yu, C., Jang, W., Kim, D., Yao, Z., ... & Majumdar, A. (2003). Measuring thermal and thermoelectric properties of one-dimensional nanostructures using a microfabricated device. J. Heat Transfer, 125(5), 881-888.

[178] Kim, P., Shi, L., Majumdar, A., & McEuen, P. L. (2001). Thermal transport measurements of individual multiwalled nanotubes. Physical review letters, 87(21), 215502.

[179] Xu, X., Pereira, L. F., Wang, Y., Wu, J., Zhang, K., Zhao, X., ... & Hong, B. H. (2014). Length-dependent thermal conductivity in suspended single-layer graphene. Nature communications, 5(1), 1-6.

[180] Jang, W., Bao, W., Jing, L., Lau, C. N., & Dames, C. (2013). Thermal conductivity of suspended few-layer graphene by a modified T-bridge method. Applied Physics Letters, 103(13), 133102.

[181] Jauregui, L. A., Yue, Y., Sidorov, A. N., Hu, J., Yu, Q., Lopez, G., Jalilian, R., Benjamin, D. K., Delkd, D. A. & Wu, W. Thermal transport in graphene nanostructures: Experiments and simulations. Ecs Transactions 28, 73-83 (2010).

[182] Chen, S., Moore, A. L., Cai, W., Suk, J. W., An, J., Mishra, C., ... & Ruoff, R. S. (2011). Raman measurements of thermal transport in suspended monolayer graphene of variable sizes in vacuum and gaseous environments. ACS nano, 5(1), 321-328.

[183] Sullivan, S., Vallabhaneni, A., Kholmanov, I., Ruan, X., Murthy, J., & Shi, L. (2017). Optical generation and detection of local nonequilibrium phonons in suspended graphene. Nano letters, 17(3), 2049-2056.

[184] Xiao, N., Dong, X., Song, L., Liu, D., Tay, Y., Wu, S., ... & Huang, W. (2011). Enhanced thermopower of graphene films with oxygen plasma treatment. Acs Nano, 5(4), 2749-2755.

[185] Oh, J., Yoo, H., Choi, J., Kim, J. Y., Lee, D. S., Kim, M. J., ... & Lee, S. S. (2017). Significantly reduced thermal conductivity and enhanced thermoelectric properties of single-and bi-layer graphene nanomeshes with sub-10 nm neck-width. Nano Energy, 35, 26-35.

[186] Dongchao Xu, Shuang Tang, Xu Du, Qing Hao, Detecting the Major Charge-Carrier Scattering Mechanism in Graphene Antidot Lattices, Carbon 144, 601-607 (2019).

[187] Xu, D., Wang, Q., Wu, X., Zhu, J., Zhao, H., Xiao, B., ... & Hao, Q. (2018). Largely reduced cross-plane thermal conductivity of nanoporous In 0.1 Ga 0.9 N thin films directly grown by metal organic chemical vapor deposition. Frontiers in Energy, 12(1), 127-136.

[188] Hu, S., Zhang, Z., Jiang, P., Ren, W., Yu, C., Shiomi, J., & Chen, J. (2019). Disorder limits the coherent phonon transport in two-dimensional phononic crystal structures. Nanoscale, 11(24), 11839-11846.

[189] Liu, F., Wang, Z., Nakanao, S., Ogawa, S., Morita, Y., Schmidt, M., ... & Mizuta, H. (2020). Conductance Tunable Suspended Graphene Nanomesh by Helium Ion Beam Milling. Micromachines, 11(4), 387.

[190] Wang, H., Kurata, K., Fukunaga, T., Takamatsu, H., Zhang, X., Ikuta, T., ... & Takata, Y. (2016). In-situ measurement of the heat transport in defect-engineered free-standing single-layer graphene. Scientific reports, 6(1), 1-7.

[191] Kang, M. S., Kang, S. Y., Lee, W. Y., Park, N. W., Kwon, K. C., Choi, S., ... & Jang, H. W. (2020). Large-scale MoS_2 thin films with chemically formed holey structure for enhanced Seebeck thermopower and their anisotropic properties. Journal of Materials Chemistry A.

[192] Li, Q. Y., Zhang, X., & Hu, Y. D. (2014). Laser flash Raman spectroscopy method for thermophysical characterization of 2D nanomaterials. Thermochimica acta, 592, 67-72.

[193] Li, Q. Y., Ma, W. G., & Zhang, X. (2016). Laser flash Raman spectroscopy method for characterizing thermal diffusivity of supported 2D nanomaterials. International Journal of Heat and Mass Transfer, 95, 956-963.

[194] Sullivan, S., Vallabhaneni, A., Kholmanov, I., Ruan, X., Murthy, J., & Shi, L. (2017). Optical generation and detection of local nonequilibrium phonons in suspended graphene. Nano letters, 17(3), 2049-2056.

[195] Vallabhaneni, A. K., Singh, D., Bao, H., Murthy, J., & Ruan, X. (2016). Reliability of Raman measurements of thermal conductivity of single-layer graphene due to selective electron-phonon coupling: A first-principles study. Physical Review B, 93(12), 125432.

[196] Li, Q. Y., Feng, T., Okita, W., Komori, Y., Suzuki, H., Kato, T., Kaneko, T., Ikuta, T., Ruan, X., Takahashi, K. (2019). Enhanced Thermoelectric Performance of As-Grown Suspended Graphene Nanoribbons. ACS Nano, 13(8), 9182-9189.

[197] Li, Q. Y., Takahashi, K., Ago, H., Zhang, X., Ikuta, T., Nishiyama, T., & Kawahara, K. (2015). Temperature dependent thermal conductivity of a suspended submicron graphene ribbon. Journal of Applied Physics, 117(6), 065102.

[198] Md Sharafat Hossain, Duc Hau Huynh, Phuong Duc Nguyen, Liming Jiang, Thanh Cong Nguyen, Feras Al-Dirini, Faruque M. Hossain, Efstratios Skafidas. Enhanced thermoelectric performance of graphene nanoribbon-based devices. Journal of Applied Physics 2016, 119 (12), 125106. DOI: 10.1063/1.4944710.

[199] Han, M. Y., Özyilmaz, B., Zhang, Y., & Kim, P. (2007). Energy band-gap engineering of graphene nanoribbons. Physical review letters, 98(20), 206805.

[200] Bae, M. H., Li, Z., Aksamija, Z., Martin, P. N., Xiong, F., Ong, Z. Y., ... & Pop, E. (2013). Ballistic to diffusive crossover of heat flow in graphene ribbons. Nature communications, 4(1), 1-7.

[201] C. Kamal, M. Ezawa, Arsenene: Two-dimensional buckled and puckered honeycomb arsenic systems, Phys. Rev. B - Condens. Matter Mater. Phys. 91 (2015) 1–10. https://doi.org/10.1103/PhysRevB.91.085423.

[202] Li, Q. Y., Zhang, X., & Takahashi, K. (2018). Variable-spot-size laser-flash Raman method to measure in-plane and interfacial thermal properties of 2D van der Waals heterostructures. International Journal of Heat and Mass Transfer, 125, 1230-1239.

[203] Vaziri, S., Yalon, E., Rojo, M. M., Suryavanshi, S. V., Zhang, H., McClellan, C. J., ... & Deshmukh, S. (2019). Ultrahigh thermal isolation across heterogeneously layered two-dimensional materials. Science advances, 5(8), eaax1325.

[204] Chen, C. C., Li, Z., Shi, L., & Cronin, S. B. (2015). Thermoelectric transport across graphene/hexagonal boron nitride/graphene heterostructures. Nano Research, 8(2), 666-672.

[205] Mahapatra, P. S., Sarkar, K., Krishnamurthy, H. R., Mukerjee, S., & Ghosh, A. (2017). Seebeck coefficient of a single van der Waals junction in twisted bilayer graphene. Nano letters, 17(11), 6822-6827.

[206] Poudel, N., Liang, S. J., Choi, D., Hou, B., Shen, L., Shi, H., ... & Cronin, S. (2017). Cross-plane thermoelectric and thermionic transport across Au/h-BN/graphene heterostructures. Scientific reports, 7(1), 1-8.

[207] Chen, C. C.; Li, Z.; Shi, L.; Cronin, S. B. Thermal interface conductance across a graphene/hexagonal boron nitride heterojunction. Appl. Phys. Lett. 2014, 104, 081908.

[208] Oh, J., Kim, Y., Chung, S., Kim, H., & Son, J. G. (2019). Fabrication of a MoS_2/Graphene Nanoribbon Heterojunction Network for Improved Thermoelectric Properties. Advanced Materials Interfaces, 6(23), 1901333.

[209] Lee, C., Hong, J., Whangbo, M. H., & Shim, J. H. (2013). Enhancing the thermoelectric properties of layered transition-metal dichalcogenides 2H-MQ2 (M= Mo, W; Q= S, Se, Te) by layer mixing: Density functional investigation. Chemistry of Materials, 25(18), 3745-3752.

[210] Wang, X., Zebarjadi, M., & Esfarjani, K. (2018). High-performance solid-state thermionic energy conversion based on 2D van der Waals heterostructures: A first-principles study. Scientific reports, 8(1), 1-9.

[211] Ding, G., Wang, C., Gao, G., Yao, K., Dun, C., Feng, C., ... & Zhang, G. (2018). Engineering of charge carriers via a two-dimensional heterostructure to enhance the thermoelectric figure of merit. *Nanoscale*, *10*(15), 7077-7084.

[212] Snyder, G. J., & Snyder, A. H. (2017). Figure of merit ZT of a thermoelectric device defined from materials properties. Energy & Environmental Science, 10(11), 2280-2283.

[213] J. Wu, Y. Liu, Y. Liu, Y. Cai, Y. Zhao, H.K. Ng, K. Watanabe, T. Taniguchi, G. Zhang, C.-W. Qiu, D. Chi, A.H.C. Neto, J.T.L. Thong, K.P. Loh, K. Hippalgaonkar, Large enhancement of thermoelectric performance in MoS_2/*h*-BN heterostructure due to vacancy-induced band hybridization, Proc. Natl. Acad. Sci. (2020) 202007495. https://doi.org/10.1073/pnas.2007495117.

[214] Ge, Y., Wan, W., Ren, Y., & Liu, Y. Large thermoelectric power factor of high-mobility 1T" phase of transition-metal dichalcogenides. PHYSICAL REVIEW RESEARCH 2, 013134 (2020)

[215] Deng, S., Li, L., Guy, O. J., & Zhang, Y. (2019). Enhanced thermoelectric performance of monolayer MoSSe, bilayer MoSSe and graphene/MoSSe heterogeneous nanoribbons. Physical Chemistry Chemical Physics, 21(33), 18161-18169.

[216] Dehkordi AM, Zebarjadi M, He J, Tritt TM (2015) Thermoelectric power factor: Enhancement mechanisms and strategies for higher performance thermoelectric materials. Mater Sci Eng Rep 97:1–22. 31.

[217] Sadeghi, H., Sangtarash, S., & Lambert, C. J. (2016). Cross-plane enhanced thermoelectricity and phonon suppression in graphene/MoS_2 van der Waals heterostructures. 2D Materials, 4(1), 015012.

[218] Ding, Z., An, M., Mo, S., Yu, X., Jin, Z., Liao, Y., ... & Yang, N. (2019). Unexpectedly high cross-plane thermoelectric performance of layered carbon nitrides. Journal of materials chemistry A, 7(5), 2114-2121.

[219] Olaya, D., Hurtado-Morales, M., Gómez, D., Castañeda-Uribe, O. A., Juang, Z. Y., & Hernández, Y. (2017). Large thermoelectric figure of merit in graphene layered devices at low temperature. 2D Materials, 5(1), 011004.

[220] Jia, P. Z., Zeng, Y. J., Wu, D., Pan, H., Cao, X. H., Zhou, W. X., ... & Chen, K. Q. (2019). Excellent thermoelectric performance induced by interface effect in MoS_2/$MoSe_2$ van der Waals heterostructure. Journal of Physics: Condensed Matter, 32(5), 055302.

[221] Yalon, E., McClellan, C. J., Smithe, K. K., Muñoz Rojo, M., Xu, R. L., Suryavanshi, S. V., ... & Pop, E. (2017). Energy dissipation in monolayer MoS_2 electronics. Nano letters, 17(6), 3429-3433.

[222] Hu, J., Wu, T., Tian, J., Klimov, N. N., Newell, D. B., & Chen, Y. P. (2017). Coulomb drag and counterflow Seebeck coefficient in bilayer-graphene double layers. Nano Energy, 40, 42-48.

[223] X. Wang, M. Zebarjadi, K. Esfarjani, First principles calculations of solid-state thermionic transport in layered van der Waals heterostructures, Nanoscale. 8 (2016) 14695–14704. https://doi.org/10.1039/C6NR02436J.

[224] A. Shakouri, J.E. Bowers, Heterostructure integrated thermionic coolers, Appl. Phys. Lett. 71 (1997) 1234. https://doi.org/10.1063/1.119861.

[225] G.D. Mahan, J.O. Sofo, M. Bartkowiak, Multilayer Thermionic Refrigerator and Generator, J. Appl. Phys. 83 (1998) 17. https://doi.org/10.1063/1.367255.

[226] G.D. Mahan, Thermionic refrigeration, J. Appl. Phys. 76 (1994) 4362–4366. https://doi.org/10.1063/1.357324.

[227] G.O. Fitzpatrick, E.J. Britt, B. Moyzhes, Updated perspective on the potential for thermionic conversion to meet 21st Century energy needs, in: IECEC-97 Proc. Thirty-Second Intersoc. Energy Convers. Eng. Conf. (Cat. No.97CH6203), IEEE, 1997: pp. 1045–1051 vol.2. https://doi.org/10.1109/IECEC.1997.661913.

[228] H. MOSS, Thermionic Diodes as Energy Converters, J. Electron. Control. 2 (1957) 305–322. https://doi.org/10.1080/00207215708937036.

[229] K. G. Hernqvist; M. Kanefsky; F. H. Norman, Thermionic energy converter, RCA. Rev. 19 (1958) 244–258.

[230] M.G. Rosul, M.S. Akhanda, M. Zebarjadi, Thermionic energy conversion, in: Nanoscale Energy Transp., IOP Publishing, 2020: pp. 14-1-14–29. https://doi.org/10.1088/978-0-7503-1738-2ch14.

[231] M. Zebarjadi, Solid-State Thermionic Power Generators: An Analytical Analysis in the Nonlinear Regime, Phys. Rev. Appl. 8 (2017) 014008. https://doi.org/10.1103/PhysRevApplied.8.014008.

[232] X. Wang, M. Zebarjadi, K. Esfarjani, High-Performance Solid-State Thermionic Energy Conversion Based on 2D van der Waals Heterostructures : A First-Principles Study, Sci. Rep. 8 (2018) 1–9. https://doi.org/10.1038/s41598-018-27430-0.

[233] S.-J. Liang, B. Liu, W. Hu, K. Zhou, L.K. Ang, Thermionic Energy Conversion Based on Graphene van der Waals Heterostructures, Sci. Rep. 7 (2017) 46211. https://doi.org/10.1038/srep46211.

[234] H. Sadeghi, S. Sangtarash, C.J. Lambert, Cross-plane enhanced thermoelectricity and phonon suppression in graphene/MoS_2 van der Waals heterostructures, 2D Mater. 4 (2016) 015012. https://doi.org/10.1088/2053-1583/4/1/015012.

[235] D.G. Cahill, Analysis of heat flow in layered structures for time-domain thermoreflectance, Rev. Sci. Instrum. 75 (2004) 5119–5122. https://doi.org/10.1063/1.1819431.

[236] K.M. Freedy, T. Zhu, D.H. Olson, P.M. Litwin, P. Hopkins, M. Zebarjadi, S.J. McDonnell, Interface chemistry and thermoelectric characterization of Ti and TiOx Contacts to MBE-Grown WSe_2, 2D Mater. (2020). https://doi.org/10.1088/2053-1583/ab834b.

[237] M.G. Rosul, D. Lee, D.H. Olson, N. Liu, X. Wang, P.E. Hopkins, K. Lee, M. Zebarjadi, Thermionic transport across gold-graphene-WSe_2 van der Waals heterostructures, Sci. Adv. 5 (2019) eaax7827. https://doi.org/10.1126/sciadv.aax7827.

[238] Lim, J., Wang, H. T., Tang, J., Andrews, S. C., So, H., Lee, J., ... & Yang, P. (2016). Simultaneous thermoelectric property measurement and incoherent phonon transport in holey silicon. ACS nano, 10(1), 124-132.

[239] Mahmood, J., Lee, E. K., Jung, M., Shin, D., Jeon, I. Y., Jung, S. M., ... & Park, N. (2015). Nitrogenated holey two-dimensional structures. Nature communications, 6(1), 1-7.

[240] Mahmood, J., Lee, E. K., Jung, M., Shin, D., Choi, H. J., Seo, J. M., ... & Park, N. (2016). Two-dimensional polyaniline (C3N) from carbonized organic single crystals in solid state. Proceedings of the National Academy of Sciences, 113(27), 7414-7419.

[241] Fischbein, M. D., & Drndić, M. (2008). Electron beam nanosculpting of suspended graphene sheets. Applied physics letters, 93(11), 113107.

[242] Russo, C. J., & Golovchenko, J. A. (2012). Atom-by-atom nucleation and growth of graphene nanopores. Proceedings of the National Academy of Sciences, 109(16), 5953-5957.

[243] Dyck, O., Ziatdinov, M., Lingerfelt, D. B., Unocic, R. R., Hudak, B. M., Lupini, A. R., ... & Kalinin, S. V. (2019). Atom-by-atom fabrication with electron beams. Nature Reviews Materials, 4(7), 497-507.

[244] Fujii, S., Yokoi, T., Fisher, C. A., Moriwake, H., & Yoshiya, M. (2020). Quantitative prediction of grain boundary thermal conductivities from local atomic environments. Nature communications, 11(1), 1-10.

[245] Zhang, H., Hippalgaonkar, K., Buonassisi, T., Løvvik, O. M., Sagvolden, E., & Ding, D. Machine Learning for Novel Thermal-Materials Discovery: Early Successes, Opportunities, and Challenges. ES Energy Environ., 2018, 2, 1–8.

[246] Lang Wu, Yue Xiao, M. Ghosh, Qiang Zhou, Qing Hao, "Machine Learning Prediction for Bandgaps of Inorganic Materials," ES Mater. Manuf. 9, 3 (2020).

[247] Mueller, T., Hernandez, A., & Wang, C. (2020). Machine learning for interatomic potential models. The Journal of Chemical Physics, 152(5), 050902.

[248] Mortazavi, B., Podryabinkin, E. V., Roche, S., Rabczuk, T., Zhuang, X., & Shapeev, A. V. (2020). Machine-learning interatomic potentials enable first-principles multiscale modeling of lattice thermal conductivity in graphene/borophene heterostructures. Materials Horizons. https://doi.org/10.1039/D0MH00787K

[249] Qian, X., Peng, S., Li, X., Wei, Y., & Yang, R. (2019). Thermal conductivity modeling using machine learning potentials: application to crystalline and amorphous silicon. Materials Today Physics, 10, 100140.